Experimental and Theoretical Studies of Novel Magnetic Behaviors in Amorphous Ferrimagnets

Chung Ting Ma
Brooklyn, NY

Bachelor of Science, Stony Brook University, 2012

A Thesis presented to the Graduate Faculty
of the University of Virginia in Candidacy for the Degree of
Doctor of Philosophy

Department of Physics

University of Virginia
December, 2019

Acknowledgment

This thesis would not be possible without the support and assistance of many people. First, I would like to express my gratitude to my advisor, Prof. S. Joseph Poon, for his guidance and mentoring throughout my graduate study at University of Virginia. He has been incredibly supportive and encouraging and provided insightful feedback on my work.

Second, I would like to thank Prof. Avik Ghosh for stimulating discussions and guidance to make my thesis possible.

Third, I would like to thank the rest of my committee members: Professor Gia-Wei Chern and Professor Utpal Chatterjee, for taking the time with insightful comments and questions.

Forth, I would like to thank all the current and former members of the Poon's group and others for collaborating and assisting during my thesis work, include Dr. Xiaopu Li, Dr. Linqiang Luo, Dr. Salinporn Kittiwatanakul, Dr. Yuan Wang, Dr. Sheng Gao, Dr. Yunkun Xie, Dr. Jianhua Ma, Wei Zhou, Hamed Vakilitaleghani, Jie Qi, and Xixiao Hu.

Fifth, I would like to thank our collaborator, Dr. Brian J. Kirby, at the National Institute of Standards and Technology for stimulating discussions during our collaborations.

Finally, my thanks go to my family for their love and support throughout my life.

List of Tables

List of Figures

Abstract

Amorphous rare-earth (RE) transition-metal (TM) alloys are ferrimagnetic (FiM) materials. In RE-TM, magnetic moments in RE and TM couples antiferromagnetically and form two magnetic sublattices. With the two sublattices, the magnetic properties of RE-TM thin films can vary significantly with temperature, composition, and thickness. For example, the magnetization of RE-TM alloys vanishes at the compensation temperature (T_{comp}). Such flexibility has both advantages and disadvantages. On the one hand, their properties can be tuned for specific applications, such as magneto-optical recording devices and skyrmion based devices. On the other hand, with so many tunable parameters, it could be very time consuming to optimize their properties experimentally. Guidance from simulations can provide crucial knowledge to reduce the time and the cost of experiments.

This thesis focuses on the tuning of magnetic properties in RE-TM thin films through simulations and experiments. Based on experimental results, computational models are developed. Then, simulations results can be used to guide experiments. In this study, RE-TM thin films were deposited on various substrates by radio frequency (RF) magnetron sputtering at room temperature. In TbFeCo on thermally oxidized Si substrates, the exchange bias effect was revealed near T_{comp}. Magnetic modeling was needed to investigate the origin of the exchange bias effect. To study this effect, the micromagnetic model is adopted into the two-sublattice model, where each sublattice evolves under its own Landau-Lifshitz-Gilbert (LLG) equation. Using the two-sublattice model, exchange interactions between two nanoscale amorphous phases were found to be the origin of the

exchange bias. Using this model, one can explore different FiM heterostructure to develop desirable exchange bias properties for applications at room temperature.

In addition to exchange bias, the ability to control magnetic anisotropy can provide great flexibility in writing and storing information. Using TbFeCo deposited on Kapton, the magnetic properties of TbFeCo are varied through the bending of Kapton. Furthermore, in VO_2/TbFeCo heterostructure, a decrease in magnetic anisotropy in TbFeCo was found to correspond to the tensile strain from the structural transition of the underlying VO_2 films. These results provide guidance on tuning magnetic anisotropy through interfacial strain.

Amorphous RE-TM thin films are also promising materials for hosting magnetic skyrmions, which are proposed for magnetic memory devices to improve density and efficiency. In RE-TM thin films, skyrmions are stabilized through the interfacial Dzyaloshinskii-Moriya Interaction (DMI), originates from an adjacent heavy metal layer. In this study, computational models are employed to investigate room-temperature skyrmions in GdCo thin films. Using atomistic simulations, various parameters, including thickness, composition, anisotropy, and interfacial DMI, are varied to explore their effects on skyrmions. Results show that increasing thickness and reducing interfacial DMI in GdCo can further reduce the size of skyrmion at room temperature, which is crucial for applications.

1. Introduction

1.1. Motivation

Amorphous ferrimagnetic (FiM) rare earth (RE) transitional metal (TM) thin films have been widely investigated for their potential applications in high-density low-current spintronics devices [1-4]. There are several advantages in using FiM RE-TM thin films for spintronics applications, including tunable magnetization and perpendicular magnetic anisotropy (PMA) [5-7]. In magnetic memory devices, having small magnetization and large PMA can greatly improve the storage time for long term data retention [8-9]. Moreover, RE-TE thin films can be synthesized at room temperature, requiring no epitaxial growth [10]. All these properties make RE-TM films promising materials for applications in spintronics devices.

Furthermore, all-optical switching (AOS) using ultrafast lasers were discovered in RE-TM thin films [11-15]. Due to their two sublattices, RE-TM films have two different time scale of interaction, which allows the switching of RE-TM through ultrafast lasers. The capability of using a laser to switch magnetic moments provides an additional method to write information in devices. Recently, small skyrmions approaching 10 nm were found in Pt/GdCo/TaO_x [16], which can potentially advance memory density and efficiency. With all these potential applications, an extensive study of FiM RE-TM is needed to obtain desirable magnetic properties for applications. With many tunable parameters, such as thickness, composition, and anisotropy, numerical simulations are needed to guide experiments to reduce the time for material explorations.

1.2. Outline

This thesis is composed of seven chapters. Chapter 1 introduced the motivations for the study of amorphous ferrimagnetic rare earth transitional metal thin films. Chapter 2 presents the experimental tools employed in this study, includes magnetron sputtering, magnetic properties measurement, and structural characterizations. Chapter 3 reveals the details of modeling methods used in this study, includes the micromagnetic model, the derivation of the two-sublattice model, and the atomistic model.

Chapter 4 investigates the exchange bias in TbFeCo thin films. Using the two sub-lattice model, experimental and simulation results are found to be in agreements. and the exchange bias in TbFeCo is proven to originate from the existence of two amorphous nanoscale phases. Chapter 5 focuses on the tuning of magnetic anisotropy in TbFeCo through interfacial strain, such as substrate bending and structural transition from a VO_2 underlayer. Chapter 6 explores the optimization of room-temperature skyrmions in GdCo through an atomistic model. Tuning of thickness and composition of GdCo is found to have a great effect on obtaining small skyrmions at room temperature.

Furthermore, experiments reveal interfacial mixings in Pt/GdCo thin films. Simulations find that skyrmions remain robust despite interfacial mixings. Finally, Chapter 7 will summarize the findings in this study and propose future works.

2. Experimental Procedures

2.1. Introduction

This chapter presents brief descriptions of the experimental techniques used in this study. Amorphous RE-TM thin films in this study were prepared by radio frequency (RF) magnetron sputtering. Magnetic properties at various temperatures were characterized by a vibrating sample magnetometer (VSM). Magneto-transport measurements were measured through anomalous Hall Effect using the Van der Pauw method **[**17]. Thickness measurements were performed by X-ray reflectivity (XRR) technique.

2.2. Magnetron Sputtering

Magnetron sputtering is a sputtering deposition technique commonly used for the deposition of thin films. Similar to other sputtering deposition, a negative charge (cathode) is applied to a target to attract the positively charged gas atoms, such as argon, to initiate the sputtering process. The gas atoms collide with the target at high velocity and bombard atoms off the target [18]. Magnetron sputtering makes use of a magnetic field to trap electrons near the surface of the target and increase the deposition rate compared to the standard sputtering technique [19]. To avoid charge build-up near the target, radio frequency (RF) sputtering is employed.

The magnetron sputtering system used in this study is shown in Figure 2.1**.** The base pressure of the system is maintained at 10^{-7} torr through a cyro-pump. The main sputtering chamber can hold up to four targets. Up to three targets can be sputtered at the same time. A load lock chamber is used for loading samples for deposition. In this study, argon is used for sputtering deposition. To initiate the sputtering process, the pressure is

raised to 20 mtorr by the flow of argon gas. Then, the pressure is gradually reduced to the deposition pressure of 7 mtorr.

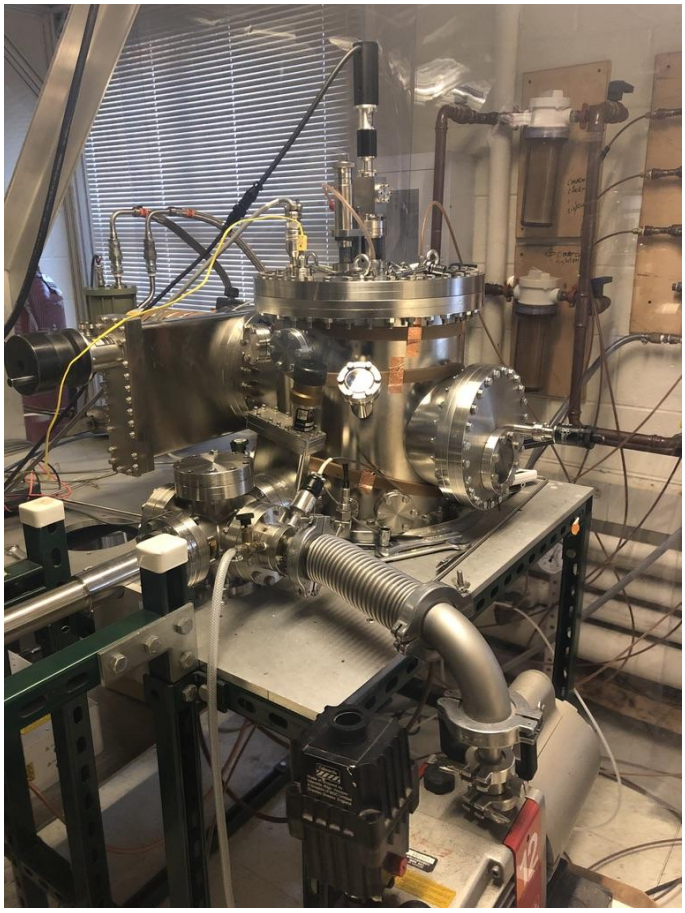

Figure 2.1 The magnetron sputtering system used in this study.

2.3. Magnetic Properties Measurement

2.3.1. Vibrating Sample Magnetometer (VSM)

Vibrating sample magnetometer (VSM) was invented by Simon Foner at MIT Lincoln Laboratory in 1955 [20]. VSM makes use of Faraday's Law of Induction to measure magnetic properties. In VSM, a sample is placed in a uniform magnetic field and vibrated to generate a change in magnetic flux. Pickup coils are used to record the induced voltage, which is proportional to the sample's magnetic moment.

In this study, a Quantum Design VersaLab™ system, as shown in Figure 2.3, was used to measure magnetic properties includes hysteresis loops and magnetization. This system is capable of generating a magnetic field of up to 3 T and has a measurement temperature range from 50 K to 400 K. In-plane and out-of-plane hysteresis loops are measured by orientating the sample parallel and perpendicular to the uniform field respectively.

Figure 2.2 Quantum Design VersaLab™ system used in this study, includes VSM and magneto-transport measurements.

2.3.2 Magneto-Transport Measurements

Anomalous Hall Effect (AHE) is another method to measure magnetic properties in thin films. In magnetic materials, the Hall resistivity is dominated by the AHE component,

which depends directly on the magnetic moment [21]. This means that AHE can be used to measure hysteresis loops of a sample. In this study, the Van der Pauw method [17] is employed to measure the Hall effect of thin films. Figure 2.4 shows an example of the Van der Pauw method. To measure AHE, a current is applied across a sample, and the voltage difference is measured perpendicular to the applied current. For example, in Figure 2.4, a current is applied from point A to D, and the voltage difference between B and C is measured to determine the Hall resistivity. This measurement is also conducted using the Quantum Design VersaLab™ system.

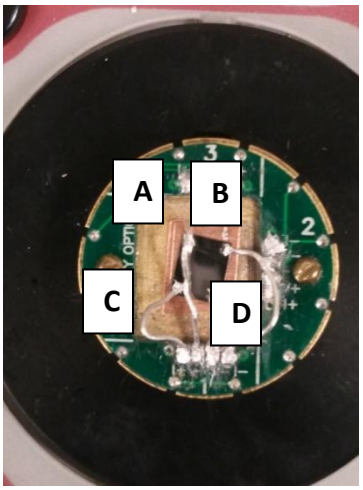

Figure 2.3 An example of a sample measured with the Van der Pauw method.

2.4 Structural Characterization

2.4.1 X-Ray Reflectometry (XRR)

X-Ray Reflectometry (XRR) is a commonly used technique to perform thickness measurements of thin films. The reflectivity profile is obtained by a small range of incident angles, typically from 0 to 5 °. In this study, a Rigaku SmartLab® was used for all XRR measurements. During operation, X-Ray source is set to an accelerating potential of 44 keV and a current of 40 A. The X-ray source generates Cu Kα radiation with a

wavelength of 1.541 Å. For analysis, reflectivity profiles were fitted using the Rigaku GXRR software to determine the sample's thickness.

3. Modeling Methods

3.1 The Landau-Lifshitz-Gilbert (LLG) Equation

In this study, simulations employed the following stochastic Landau-Lifshitz-Gilbert (LLG) equation [22] to evolve magnetic moment **M**.

$$\frac{d\boldsymbol{M}}{dt} = -\frac{\gamma}{1+\alpha^2}\boldsymbol{M} \times \left(\boldsymbol{H_{eff}} + \boldsymbol{\xi}\right) - \frac{\gamma\alpha}{(1+\alpha^2)M_s}\boldsymbol{M} \times \left[\boldsymbol{M} \times \left(\boldsymbol{H_{eff}} + \boldsymbol{\xi}\right)\right]$$

where γ is the gyromagnetic ratio, α is the Gilbert damping constant, $\boldsymbol{H_{eff}}$ is the effective field, $\boldsymbol{\xi}$ is the Gaussian white noise term for thermal fluctuations, and M_s is the saturation magnetization.

The effective field $\boldsymbol{H_{eff}}$ is given by the first derivative of the spin Hamiltonian H [23]

$$\boldsymbol{H_{eff}} = -\frac{1}{\mu_s}\frac{\delta H}{\delta \boldsymbol{m}}$$

where μ_s is the magnetic moment, and $\boldsymbol{m}$ = **M**/μ_s is the reduced magnetic moment.

In this study, different models are employed to evaluate the effective field $\boldsymbol{H_{eff}}$. In the following section, we will explore the use of the micromagnetic model, the two-sublattice model, and the atomistic model to evaluate $\boldsymbol{H_{eff}}$.

3.2 Micromagnetic Model

In a magnetic simulation, treating each spin as individual spins can become very time consuming for large scale simulation. One technique to reduce simulation time is the micromagnetic model [24]. In the micromagnetic model, instead of treating each spin as individual spins, multiple spins are combined as one continuous magnetization **M**. This is

known as the continuum hypothesis. An important constraint for this hypothesis is that the magnetization **M** needs to be smooth, which is reflected in the following continuum approximation in exchange interaction.

In the atomistic model, the exchange interaction E_{ij} between a neighboring pair of spin at site i and j is given by the following classical Heisenberg Model

$$E_{ij} = -\frac{1}{2} J_{ij} \boldsymbol{M_i} \cdot \boldsymbol{M_j} = -\frac{1}{2} J_{ij} M^2 cos\theta_{ij}$$

where J_{ij} is the exchange constant between site i and j, $\mathbf{M_i} and \boldsymbol{M_j}$ are the magnetic moment at site i and j respectively, $\theta_{ij}$is the angle between the magnetic moment at site i and j.

For small angle, i.e., close to a uniform magnetic moment between site i and j, expanding $cos\theta_{ij}$to the leading order, the exchange energy can be approximated as follows

$$E_{ij} \approx \text{ JM}^2\theta_{ij}^2 + constant$$

Further approximation can be made using the reduced magnetization $\boldsymbol{m_i} = \frac{\mathbf{M_i}}{\mathbf{Ms}}$. For small angle, $\left|\theta_{ij}\right| \approx \left|\boldsymbol{m_i} - \boldsymbol{m_j}\right|$. Thus, exchange energy can be written as

$$E_{ij} \approx \text{JM}^2\left(\boldsymbol{m_i} - \boldsymbol{m_j}\right)^{\mathbf{2}}$$

In the continuum approximation,

$$\boldsymbol{m_i} - \boldsymbol{m_j} \approx \boldsymbol{r_{ij}} \cdot \boldsymbol{\nabla m}$$

where $\boldsymbol{r_{ij}} = x_{ij}\hat{\boldsymbol{x}} + y_{ij}\hat{y} + z_{ij}\hat{z}$ is the position vector of site j with respect to site i.

Substitute this back into exchange energy E_{ij}

$$E_{ij} \approx JS^2[(\boldsymbol{r_{ij}} \cdot \boldsymbol{\nabla m_x})^2 + (\boldsymbol{r_{ij}} \cdot \boldsymbol{\nabla m_y})^2 + (\boldsymbol{r_{ij}} \cdot \boldsymbol{\nabla m_z})^2]$$

To obtain the exchange energy per unit volume $E_{exchange}$, we need to sum over all the neighbor j. This sum is different for different structures. For example, in a cubic lattice, because of symmetry,

$$\sum_j x_{ij}y_{ij} = \cdots = 0\,,\ \sum_j x_{ij}^2 = \cdots = \frac{1}{3}\sum_j r_{ij}^2$$

The exchange energy per unit volume $E_{exchange}$ is given by the following

$$E_{exchange} = \frac{1}{2}(\frac{1}{3}nJM^2)\sum_j r_{ij}^2[(\boldsymbol{\nabla m_x})^2+(\boldsymbol{\nabla m_y})^2+(\boldsymbol{\nabla m_z})^2])$$

where n is the number of nearest neighbor, and in general, exchange energy per unit volume $E_{exchange}$ is given by

$$E_{exchange} = A[(\boldsymbol{\nabla m_x})^2+(\boldsymbol{\nabla m_y})^2+(\boldsymbol{\nabla m_z})^2]$$

where A is the exchange stiffness constant.

Thus, the total exchange energy E_{Tot-ex} in the micromagnetic model is given by the following volume integral

$$E_{Tot-ex} = \int_V \mathrm{A}\,[(\boldsymbol{\nabla} m_x)^2 + (\boldsymbol{\nabla} m_y)^2 + (\boldsymbol{\nabla} m_z)^2]dV$$

For the other energy, the conversion to micromagnetic is very straight forward and can relate directly with the atomistic model.

The anisotropy energy from uniaxial anisotropy E_{Tot-K} is given by

$$E_{Tot-K} = \int_V \mathrm{K}\,(1 - \cos\theta_\mathrm{K})^2\, dV$$

where K is uniaxial anisotropy constant and θ_K is the angle between anisotropy and the magnetic moment

The Zeeman energy from an applied field E_{Tot-Ap} is given by

$$E_{Tot-ap} = -\int_V \mu_0 \boldsymbol{M} \cdot \boldsymbol{H_{ap}}\, dV$$

where $\mu_0$is the vacuum permeability and $\boldsymbol{H_{ap}}$ is the applied field

The demagnetization energy $E_{Tot-Demag}$ is given by

$$E_{Tot-demag} = -\int_V \frac{1}{2}\mu_0 \boldsymbol{M} \cdot \boldsymbol{H_{demag}}\, dV$$

where $\boldsymbol{H_{demag}}$ is the demagnetization field.

For computation, an approximation is needed to evaluate the derivative terms in the exchange energy. First, the integral is discretized and using the identity $|\nabla f|^2 = \nabla \cdot (f\nabla f) - f\nabla^2 f$. The exchange energy$E_{Tot-ex}$ is rewritten as follows

$$E_{Tot-ex} = -\mathrm{A}\mathbf{m} \cdot \left(\frac{\partial^2 \boldsymbol{m}}{\partial \mathrm{x}^2} + \frac{\partial^2 \boldsymbol{m}}{\partial \mathrm{y}^2} + \frac{\partial^2 \boldsymbol{m}}{\partial \mathrm{z}^2}\right)$$

To evaluate the second derivative, two different methods, finite difference [25] and finite element [26], are commonly used in the micromagnetic simulation. In this study, the micromagnetic simulations follow the Object Oriented Micro-Magnetic Framework

(OOMMF) project [27], which uses the finite difference method to approximate the second derivative terms. Under the finite difference method, the second derivative is expanded by a distance h as follows

$$\frac{\partial^2 \boldsymbol{m}(x)}{\partial x^2} \approx \frac{1}{h^2}[\boldsymbol{m}(\text{x-h})\text{-}2\mathbf{m}(\text{x})+\mathbf{m}(\text{x+h})]+\text{O}(h^2)$$

Each second derivative term is approximated by the magnetization of a cell and the two neighboring cells in that direction. In this approximation, there are totally six neighbors in all directions, so this is called "6-neighbor exchange". For cell i, with neighboring cells j, the exchange interaction is approximated as follows

$$E_{Tot-ex} \approx \sum_j A_{ij} \frac{\boldsymbol{m_i} \cdot (\boldsymbol{m_i} - \boldsymbol{m_j})}{d_{ij}^2}$$

where the distance between cell i and cell j.

For other energy, a straight forward discretization is employed for numerical evaluation

With anisotropy energy $E_{Tot-K} \approx \text{K}(1 - \cos\theta_\text{K})^2$

Energy due to applied field $E_{Tot-ap} \approx -\mu_0 \boldsymbol{M} \cdot \boldsymbol{H_{ap}}$

and demagnetization energy $E_{Tot-demag} \approx -\frac{1}{2}\mu_0 \boldsymbol{M} \cdot \boldsymbol{H_{demag}}$

Using these energy $\boldsymbol{H_{eff}}$ is computed using the following first derivative of the energy

$$\boldsymbol{H_{eff}} = -\frac{1}{M_s}\frac{\delta E}{\delta \boldsymbol{m}}$$

and magnetization **M** is evolved under the LLG equation to study the tuning of magnetic properties.

3.3 Micromagnetic Two-sublattice Model

In ferrimagnetic RE-TM thin films, the co-existence of two magnetic sublattices can be troublesome for a simple micromagnetic model discussed in section 3.1. This is because, with two sublattices, many neighboring spins are no longer close to parallel to each other, and the small-angle approximation in the continuum hypothesis is no longer valid. To address this issue, a two-sublattice model is needed to treat each sublattice separately in the micromagnetic model.

In the two-sublattice model, each cell contains a separated Tb and FeCo component, forming two antiferromagnetically coupled sublattices. Following Mansuripur [28, 29], we allow each component evolves under LLG equation.

$$\dot{\boldsymbol{M}}_{Tb} = -\gamma\left(\boldsymbol{M}_{Tb} \times \mathbf{H}_{\mathrm{eff}_{\mathrm{Tb}}}\right) + \frac{\alpha}{M_{Tb}}\left(\boldsymbol{M}_{Tb} \times \dot{\boldsymbol{M}}_{Tb}\right)$$

$$\dot{\boldsymbol{M}}_{Fe} = -\gamma\left(\boldsymbol{M}_{Fe} \times \mathbf{H}_{\mathrm{eff}_{Fe}}\right) + \frac{\alpha}{M_{Fe}}\left(\boldsymbol{M}_{Fe} \times \dot{\boldsymbol{M}}_{Fe}\right)$$

As discussed in Section 3.2, in the micromagnetic model, the effective field $\mathbf{H}_{\mathrm{eff}}$ is the sum of the external field $\mathbf{H}_{\mathrm{ext}}$, the demagnetization field $\mathbf{H}_{\mathrm{demag}}$, the anisotropy field $\mathbf{H}_{\mathrm{ani}}$, and the exchange field $\mathbf{H}_{\mathrm{exch}}$. In this model, each component has its respective effective field.

$$\mathbf{H}_{\mathrm{eff}_{\mathrm{Tb}}} = \mathbf{H}_{\mathrm{ext}_{\mathrm{Tb}}} + \mathbf{H}_{\mathrm{demag}_{\mathrm{Tb}}} + \mathbf{H}_{\mathrm{ani}_{\mathrm{Tb}}} + \mathbf{H}_{\mathrm{exch}_{\mathrm{Tb}}}$$

$$\mathbf{H}_{\mathrm{eff}_{\mathrm{Fe}}} = \mathbf{H}_{\mathrm{ext}_{\mathrm{Fe}}} + \mathbf{H}_{\mathrm{demag}_{\mathrm{Fe}}} + \mathbf{H}_{\mathrm{ani}_{\mathrm{Fe}}} + \mathbf{H}_{\mathrm{exch}_{\mathrm{Fe}}}$$

The effective external field and the effective demagnetization field are equal for each component, $\mathbf{H}_{\text{ext}} = \mathbf{H}_{\text{ext}_{\text{Tb}}} = \mathbf{H}_{\text{ext}_{\text{FeCo}}}$, and $\mathbf{H}_{\text{demag}_{\text{Tb}}} = \mathbf{H}_{\text{demag}_{\text{FeC}}}$. For the effective anisotropy field, the two components are different by the anisotropy constant of Tb, $K_{u_{Tb}}$, and FeCo, $K_{u_{Fe}}$.

For the effective exchange fields, since each sublattice interacts with itself and the other sublattice, effective exchange fields have contributions from interactions within the same sublattice, $\mathbf{H}_{\text{exch}_{\text{Tb}-\text{Tb}}}$ and $\mathbf{H}_{\text{exch}_{\text{Fe}-\text{Fe}}}$, and interactions between the two sublattices $\mathbf{H}_{\text{exch}_{\text{Tb}-\text{Fe}}}$and $\mathbf{H}_{\text{exch}_{\text{Fe}-\text{Tb}}}$.

$$\mathbf{H}_{\text{exch}_{\text{Tb}}} = \mathbf{H}_{\text{exch}_{\text{Tb}-\text{Tb}}} + \mathbf{H}_{\text{exch}_{\text{Tb}-\text{Fe}}}$$

$$\mathbf{H}_{\text{exch}_{\text{Fe}}} = \mathbf{H}_{\text{exch}_{\text{Fe}-\text{Fe}}} + \mathbf{H}_{\text{exch}_{\text{Fe}-\text{Tb}}}$$

The effective exchange fields of two neighboring components of the same type $\mathbf{H}_{\text{exch}_{\text{Tb}-\text{Tb}}}$, $\mathbf{H}_{\text{exch}_{\text{FeCo}-\text{FeCo}}}$ are identical to the usual exchange field in the micromagnetic model, proportional to the Laplacian of the respective reduced magnetization.

$$\mathbf{H}_{\text{exch}_{\text{Tb}-\text{Tb}}} = \frac{2A_{Tb-Tb}}{\mu_0 M_{Tb}} \nabla^2 \boldsymbol{m}_{Tb}$$

$$\mathbf{H}_{\text{exch}_{\text{Fe}-\text{Fe}}} = \frac{2A_{Fe-Fe}}{\mu_0 M_{Fe}} \nabla^2 \boldsymbol{m}_{Fe}$$

where $\boldsymbol{m} = \boldsymbol{M}/M_s$ is the reduced magnetization

$$A_{Tb-Tb} = \frac{1}{4} J_{Tb-Tb} S_{Tb}^2 z_{Tb-Tb} r_{nn}^2 c_{Tb}/a^3$$

$$A_{Fe-Fe} = \frac{1}{4} J_{Fe-Fe} S_{Fe}^2 z_{Fe-Fe} r_{nn}^2 c_{Fe}/a^3$$

where c_A is the element A concentration, z_{A-B} is the number of element B atoms around element A, $r_{nn}$is the distance to the nearest neighbor

The effective exchange fields between Tb and Fe are found to have two terms

$$\mathbf{H}_{\mathrm{exch_{Tb-Fe}}} = \frac{2A_{Tb-Fe}}{\mu_0 M_{Tb}} \nabla^2 \boldsymbol{m}_{Fe} + \frac{B_{Tb-Fe}}{\mu_0 \mathrm{M_{Tb}}} \boldsymbol{m}_{\mathbf{Fe}}$$

$$\mathbf{H}_{\mathrm{exch_{Fe-Tb}}} = \frac{2A_{Fe-Tb}}{\mu_0 M_{Fe}} \nabla^2 \boldsymbol{m}_{Tb} + \frac{B_{Fe-Tb}}{\mu_0 \mathrm{M_{Fe}}} \boldsymbol{m}_{\boldsymbol{Tb}}$$

where

$$A_{Tb-Fe} = \frac{1}{4} J_{Tb-Fe} S_{Tb} S_{Fe} z_{Tb-Fe} r_{nn}^2 c_{Tb} / a^3$$

$$A_{Fe-Tb} = \frac{1}{4} J_{Tb-Fe} S_{Tb} S_{Fe} z_{Fe-Tb} r_{nn}^2 c_{Fe} / a^3$$

$$B_{Tb-Fe} = J_{Tb-Fe} S_{Tb} S_{Fe} c_{Tb} z_{Tb-Fe} / a^3 = B_{Fe-Tb}$$

The detailed derivation is shown in section 3.2.1.

The total effective fields due to exchange interaction are the followings,

$$\mathbf{H}_{\mathrm{exch_{Tb}}} = \frac{2A_{Tb-Tb}}{\mu_0 M_{Tb}} \nabla^2 \boldsymbol{m}_{Tb} + \frac{2A_{Tb-Fe}}{\mu_0 M_{Tb}} \nabla^2 \boldsymbol{m}_{Fe} + \frac{B_{Tb-Fe}}{\mu_0 \mathrm{M_{Tb}}} \boldsymbol{m}_{\mathbf{Fe}}$$

$$\mathbf{H}_{\mathrm{exch_{Fe}}} = \frac{2A_{Fe-Fe}}{\mu_0 M_{Fe}} \nabla^2 \boldsymbol{m}_{Fe} + \frac{2A_{Fe-Tb}}{\mu_0 M_{Fe}} \nabla^2 \boldsymbol{m}_{Tb} + \frac{B_{Fe-Tb}}{\mu_0 \mathrm{M_{Fe}}} \boldsymbol{m}_{\boldsymbol{Tb}}$$

3.3.1 Derivation of Effective Field in the two-sublattice model

This section presents the derivation of the effective field [30], which begins from the atomistic Hamiltonian $\mathcal{H}_A$ of element A. For element A, the Hamiltonian of nearest neighbor exchange interaction between site i and site j is

$$\mathcal{H}_A = -\frac{1}{2}\sum_{<i,j>} J_{ij}\,\boldsymbol{S}_i \cdot \boldsymbol{S}_j$$

$$= -\frac{1}{2}\sum_{<Tb_i,Tb_j>} J_{Tb-Tb}\boldsymbol{S}_{Tb_i}\cdot\boldsymbol{S}_{Tb_j} - \frac{1}{2}\sum_{<Fe_i,Fe_j>} J_{Fe-Fe}\boldsymbol{S}_{Fe_i}\cdot\boldsymbol{S}_{Fe_i} - \sum_{<Tb_i,Fe_j>} J_{Tb-Fe}\boldsymbol{S}_{Tb_i}\cdot\boldsymbol{S}_{Fe_j}$$

where $\boldsymbol{S_A}$ is the moment of element A.

We can rewrite Tb-Tb and Fe-Fe terms as follow

$$\mathcal{H}_{Tb-Tb} = -\frac{1}{2}J_{Tb-Tb}S_{Tb}^2\sum_{<Tb_i,Tb_j>}\boldsymbol{m}_{Tb_i}\cdot\boldsymbol{m}_{Tb_j}$$

$$= const. + \frac{1}{4}J_{Tb-Tb}S_{Tb}^2\sum_{<Tb_i,Tb_j>}\left(\boldsymbol{m}_{Tb_i}-\boldsymbol{m}_{Tb_j}\right)^2$$

Using the continuous assumption

$$\boldsymbol{m}_{Tb_j} \approx \boldsymbol{m}_{Tb_i} + \boldsymbol{r}_{ij}\cdot\nabla\boldsymbol{m}_{Tb_i}$$

$$\mathcal{H}_{Tb-Tb} \approx \frac{1}{4}J_{Tb-Tb}S_{Tb}^2 z_{Tb-Tb} r_{nn}^2 \sum_{Tb_i}\left(\nabla\boldsymbol{m}_{Tb_i}\right)^2 = A_{Tb-Tb}\int(\nabla\boldsymbol{m}_{Tb})^2 d^3x$$

Similarly,

$$\mathcal{H}_{Fe-Fe} \approx \frac{1}{4} J_{Fe-Fe} S_{Fe}^2 z_{Fe-Fe} r_{nn}^2 \sum_{Fe_i} \left(\nabla \boldsymbol{m}_{Fe_i}\right)^2 = A_{Fe-Fe} \int (\nabla \boldsymbol{m}_{Fe})^2 d^3x$$

$A_{Tb-Tb} = \frac{1}{4} J_{Tb-Tb} S_{Tb}^2 z_{Tb-Tb} r_{nn}^2 c_{Tb}/a^3$ and $A_{Fe-Fe} = \frac{1}{4} J_{Fe-Fe} S_{Fe}^2 z_{Fe-Fe} r_{nn}^2 c_{Fe}/a^3$

The ferrimagnetic (Tb-Fe) term

$$\mathcal{H}_{Tb-Fe} = -\sum_{<Tb_i, Fe_j>} J_{Tb-Fe} \boldsymbol{S}_{Tb_i} \cdot \boldsymbol{S}_{Fe_j} = \frac{1}{2} J_{Tb-Fe} S_{Tb} S_{Fe} \sum_{<Tb_i, Fe_j>} \left(\boldsymbol{m}_{Tb_i} - \boldsymbol{m}_{Fe_j}\right)^2$$

Using the continuous assumption to expand $\boldsymbol{m}_{Fe_j}$

$$\mathcal{H}_{Tb-Fe} \approx \frac{1}{2} J_{Tb-Fe} S_{Tb} S_{Fe} \sum_{<Tb_i, Fe_j>} \left(\boldsymbol{m}_{Tb_i} - \boldsymbol{m}_{Fe_i} - \boldsymbol{r}_{ij} \cdot \nabla \boldsymbol{m}_{Fe_i} - \frac{1}{2} \boldsymbol{r}_{ij}^2 \nabla^2 \boldsymbol{m}_{Fe_i}\right)^2$$

$$\approx \frac{1}{2} J_{Tb-Fe} S_{Tb} S_{Fe} \sum_{<Tb_i, Fe_j>} \Big(\left(\boldsymbol{m}_{Tb_i} - \boldsymbol{m}_{Fe_i}\right)^2 - 2\left(\boldsymbol{m}_{Tb_i} - \boldsymbol{m}_{Fe_i}\right) \cdot \left(\boldsymbol{r}_{ij} \cdot \nabla \boldsymbol{m}_{Fe_i}\right)$$

$$- \left(\boldsymbol{m}_{Tb_i} - \boldsymbol{m}_{Fe_i}\right) \boldsymbol{r}_{ij}^2 \cdot \nabla^2 \boldsymbol{m}_{Fe_i} + \left(\boldsymbol{r}_{ij} \cdot \nabla \boldsymbol{m}_{Fe_i}\right)^2 \Big)$$

The second term $\sum_{<Tb_i, Fe_j>} \left(-2\left(\boldsymbol{m}_{Tb_i} - \boldsymbol{m}_{Fe_i}\right) \cdot \left(\boldsymbol{r}_{ij} \cdot \nabla \boldsymbol{m}_{Fe_i}\right)\right)$ vanishes with the assumption of center symmetry

Combine the last two terms,

$$\mathcal{H}_{Tb-Fe} \approx \frac{1}{2} J_{Tb-Fe} S_{Tb} S_{Fe} z_{Tb-Fe} \sum_{Tb_i} \Big(\left(\boldsymbol{m}_{Tb_i} - \boldsymbol{m}_{Fe_i}\right)^2 - r_{nn}^2 \boldsymbol{m}_{Tb_i} \cdot \nabla^2 \boldsymbol{m}_{Fe_i} + r_{nn}^2 \nabla$$

$$\cdot \left(\boldsymbol{m}_{Fe_i} \cdot \nabla \boldsymbol{m}_{Fe_i}\right) \Big)$$

$$= -B_{Tb-Fe}\int \boldsymbol{m}_{Tb}\cdot\boldsymbol{m}_{Fe}d^3x - 2A_{Tb-Fe}\int \boldsymbol{m}_{Tb}\cdot\nabla^2\boldsymbol{m}_{Fe}d^3x$$

$$+ 2A_{Tb-Fe}\oint \boldsymbol{m}_{Fe}\cdot\nabla\boldsymbol{m}_{Fe}\cdot\boldsymbol{n}dS$$

$$A_{Tb-Fe} = \frac{1}{4}J_{Tb-Fe}S_{Tb}S_{Fe}z_{Tb-Fe}r_{nn}^2c_{Tb}/a^3$$

$$A_{Fe-Tb} = \frac{1}{4}J_{Tb-Fe}S_{Tb}S_{Fe}z_{Fe-Tb}r_{nn}^2c_{Fe}/a^3$$

and $B_{Tb-Fe} = J_{Tb-Fe}S_{Tb}S_{Fe}c_{Tb}z_{Tb-Fe}/a^3 = B_{Fe-Tb}$

The total energy

$$\mathcal{H}_A = \int \big(A_{Fe-Fe}(\nabla\boldsymbol{m}_{Fe})^2 + A_{Tb-Tb}(\nabla\boldsymbol{m}_{Tb})^2 - 2A_{Tb-Fe}\boldsymbol{m}_{Tb}$$

$$\cdot\nabla^2\boldsymbol{m}_{Fe} - B_{Tb-Fe}(\boldsymbol{m}_{Tb}\cdot\boldsymbol{m}_{Fe})\big)d^3x + 2A_{Tb-Fe}\oint \boldsymbol{m}_{Fe}\nabla\boldsymbol{m}_{Fe}\cdot\boldsymbol{n}dS$$

The last term is integrated on the boundary, so the energy density is

$$\mathcal{E}_A = A_{Fe-Fe}(\nabla\boldsymbol{m}_{Fe})^2 + A_{Tb-Tb}(\nabla\boldsymbol{m}_{Tb})^2 - 2A_{Tb-Fe}\boldsymbol{m}_{Tb}\nabla^2\boldsymbol{m}_{Fe} - B_{Tb-Fe}(\boldsymbol{m}_{Tb}\cdot\boldsymbol{m}_{Fe})$$

The effective field due to exchange interaction

$$\boldsymbol{H}_{eff,Tb} = -\frac{\delta\mathcal{E}_A}{\mu_0 M_{s,Tb}\delta\boldsymbol{m}_{Tb}}$$

$$= \frac{2}{\mu_0 M_{s,Tb}}A_{Tb-Tb}\nabla^2\boldsymbol{m}_{Tb} + \frac{2}{\mu_0 M_{s,Tb}}A_{Tb-Fe}\nabla^2\boldsymbol{m}_{Fe} + \frac{1}{\mu_0 M_{s,Tb}}B_{Tb-Fe}\boldsymbol{m}_{Fe}$$

Similarly,

$$\boldsymbol{H}_{eff,Fe} = -\frac{\delta \mathcal{E}_A}{\mu_0 M_{s,Fe} \delta \boldsymbol{m}_{Fe}}$$

$$= \frac{2}{\mu_0 M_{s,Fe}} A_{Fe-Fe} \nabla^2 \boldsymbol{m}_{Fe} + \frac{2}{\mu_0 M_{s,Fe}} A_{Fe-Tb} \nabla^2 \boldsymbol{m}_{Tb} + \frac{1}{\mu_0 M_{s,Fe}} B_{Fe-Tb} \boldsymbol{m}_{Tb}$$

These effective fields are used to evolve each sublattice under the LLG equation.

3.4 Atomistic Model

In the atomistic model, every spin is accounted for in the simulations. For a ferrimagnetic system, due to the existence of two sublattices, allowing all the spins to vary can be crucial in investigating magnetic spin textures, such as skyrmions. In the atomistic model, the following classical atomistic Hamiltonian H [23] is employed to study magnetic properties

$$H = -\frac{1}{2} \sum_{<i,j>} J_{ij} \boldsymbol{s_i} \cdot \boldsymbol{s_j} - \frac{1}{2} \sum_{<i,j>} D_{ij} \cdot (\boldsymbol{s_i} \times \boldsymbol{s_j}) - K_i (\boldsymbol{s_i} \cdot \widehat{\boldsymbol{K_i}})^2$$

$$-\mu_0 \mu_i \boldsymbol{H_{ext}} \cdot \boldsymbol{s_i} - \mu_0 \mu_i \boldsymbol{H_{demag}} \cdot \boldsymbol{s_i}$$

where $\boldsymbol{s_i}, \boldsymbol{s_j}$ are the normalized spins and μ_i, μ_j are the atomic moments at sites i, j, respectively. The atomic moment is absorbed into the exchange constant, $J_{ij} = \mu_i \mu_j j_{ij}$, the DMI interaction $\boldsymbol{D_{ij}} = \mu_i \mu_j \boldsymbol{d_{ij}}$ and the effective anisotropy $K_i = \mu_i k_i$. $\boldsymbol{H_{ext}}$ and $\boldsymbol{H_{demag}}$ are the external field and demagnetization field, respectively.

4. Exchange Bias in Amorphous TbFeCo Thin Films

4.1 Introduction

In conventional magnetic materials, the hysteresis loops are symmetric along the magnetic field axis. With exchange bias, hysteresis loops are shifted along the magnetic field axis. The exchange bias effect has drawn interest in research due to their potential in device applications [31-33]. The exchange bias is commonly found in multilayers, such as ferromagnet (FM)-antiferromagnet (AFM) [34-36], FM-FM [37-38], and FM-ferrimagnet (FiM) [39-40].In these materials, the exchange anisotropy across two different layers produces the standard exchange bias effect. Besides multilayer films, intrinsic exchange bias is also reported at low temperatures in Ni-Mn-X (X = Sn, In, Sb) and Mn-Pt-Ga due to the co-existence of two magnetic regions [41-42]. The exchange bias effects involving FiM have been investigated numerically [43-46]. Monte Carlo Metropolis sampling was employed to investigate the EB effect in FM core/FiM shell structure [43]. Using the micromagnetic model, EB effects were obtained and compared to experimental results in exchange-coupled FiM/FM heterostructures [44, 45], FiM bilayers [46], and multilayers [47-49].

In this study, the exchange bias effects at room temperature in TbFeCo and TbSmFeCo films are investigated. Experiment results show a pronounced shift in hysteresis loops at room temperature. Furthermore, a micromagnetic two-sublattice model (derived in section 3.2), adopted from the micromagnetic model, is employed to study heterogeneous magnetic materials with two interpenetrating nanoscale phases. Using this model, the calculated exchange bias effects are compared to the experimental results.

4.2 Experimental Results

The exchange bias effect has been found to exist in TbFeCo films that contain two nanoscale amorphous phases [50]. As revealed by atom probe tomography, scanning transmission electron microscopy, and energy dispersive spectroscopy mapping, one phase (Phase II) corresponds to regions of FeCo enrichment and Tb depletion, while the other (Phase I) corresponds to regions of Tb enrichment and FeCo depletion. The length scales of these two phases are 2-5 nm. The exchange interaction between the two phases is believed to lead to the observed exchange bias in these TbFeCo films. More specifically, the Fe-enriched Phase II is dominated by FeCo moments at room temperature and behaves in an FM manner. On the other hand, the Tb-enriched Phase I is a near-compensated FiM with a large coercivity. When the field is not large enough to switch Phase I, Phase I provides unidirectional exchange anisotropy and affects the reversal field of Phase II. It should be noted that the exchange bias effect in this system is a minor loop effect, arising from the fact that Phase I could only be switched in a sufficiently large field. Figure 4.1 shows the experimental saturation magnetization (M_s) and coercivity (H_c) as a function of temperature. Results show that the T_{comp} of TbFeCo is near 250 K, and exchange bias is observed near the T_{comp}.

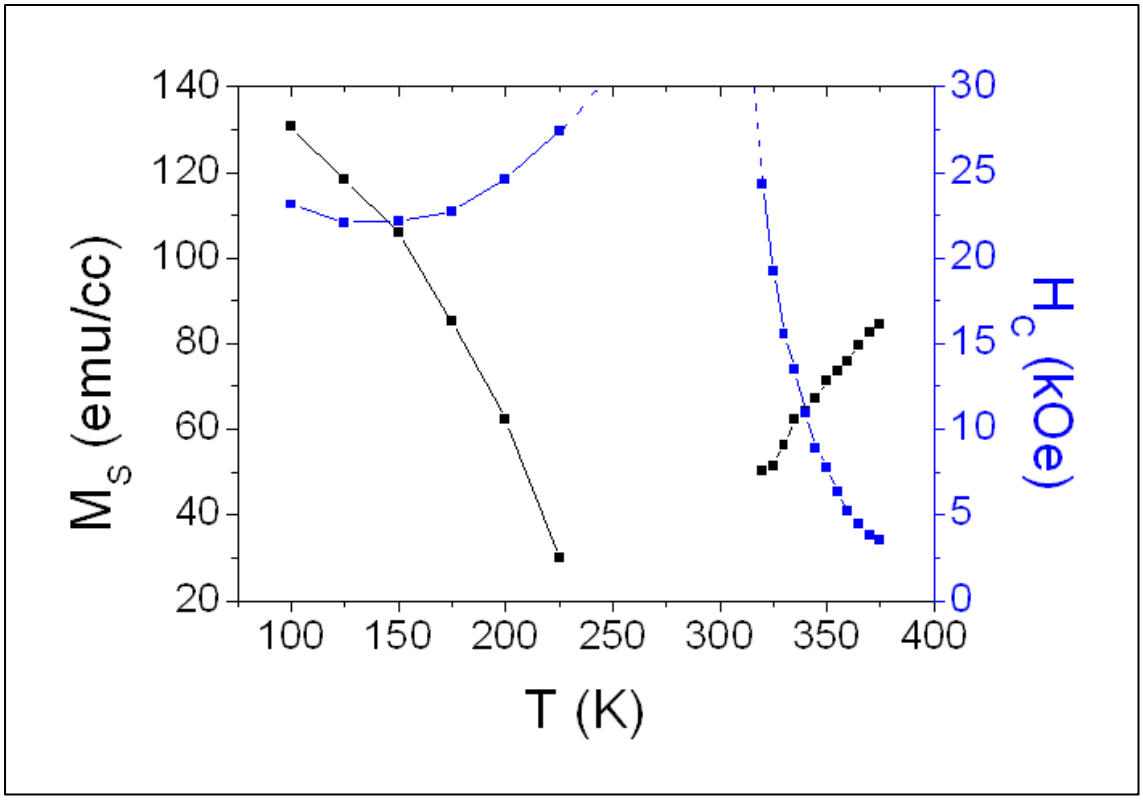

Figure 4.1 Experimental saturation magnetization (M_s) and coercivity (H_c) of TbFeCo as a function of temperature

4.2.1 Above the compensation temperature

Figure 4.2 shows the exchange bias minor loops of TbFeCo above T_{comp}. Both positive and negative exchange bias is observed at 300 K. Negative exchange bias is observed in the sample initialized at 355 K, and 3 T, then, cooled down to 300 K at zero field. The hysteresis loop is measured at 300 K from 3 T through -3 T to 3 T. At 355 K and 3 T, the FeCo moments of both Phase I and Phase II are aligned in the positive direction, parallel to the applied field. Cooling down to 300 K at zero field maintains the spin orientation for both Phase I and Phase II. At 300 K, the near-compensated phase, Phase I, has larger coercivity then 3 T. Thus, within 3 T external field, Phase I maintains its spin orientation. Since the FeCo moments in both Phase I and Phase II are orientated parallel to each other

at 3 T, an additional external field is required to reverse the moments of Phase II when going from 3 T to -3 T, resulting in negative exchange bias. The observed shift in overall magnetization originates from Phase I. Since the moments of Phase I maintain their orientations, they contribute a fixed amount to the overall magnetization of the sample. After initializing at 355K and 3T, Phase I has net positive magnetization at 300 K, resulting in a positive shift in the magnetization. Positive exchange bias is observed in the sample initialized at 175 K and 3 T, then warmed up to 300 K at zero field. At 175 K and 3 T, since it is below T_{comp} of Phase I, the FeCo moments of Phase I are aligned in the negative direction, opposite to the applied field. This initializing procedure results in the FeCo moments of Phase I (negative) and Phase II (positive) aligned opposite to each other at 300 K and 3 T. Therefore, when the external field is applied from 3 T to -3 T, Phase I provide an additional energy to flip the moments of Phase II, resulting in a positive exchange bias. The observed shift in overall magnetization is in the negative direction because the net magnetization of Phase I is negative at 300 K after initializing at 175 K and 3 T.

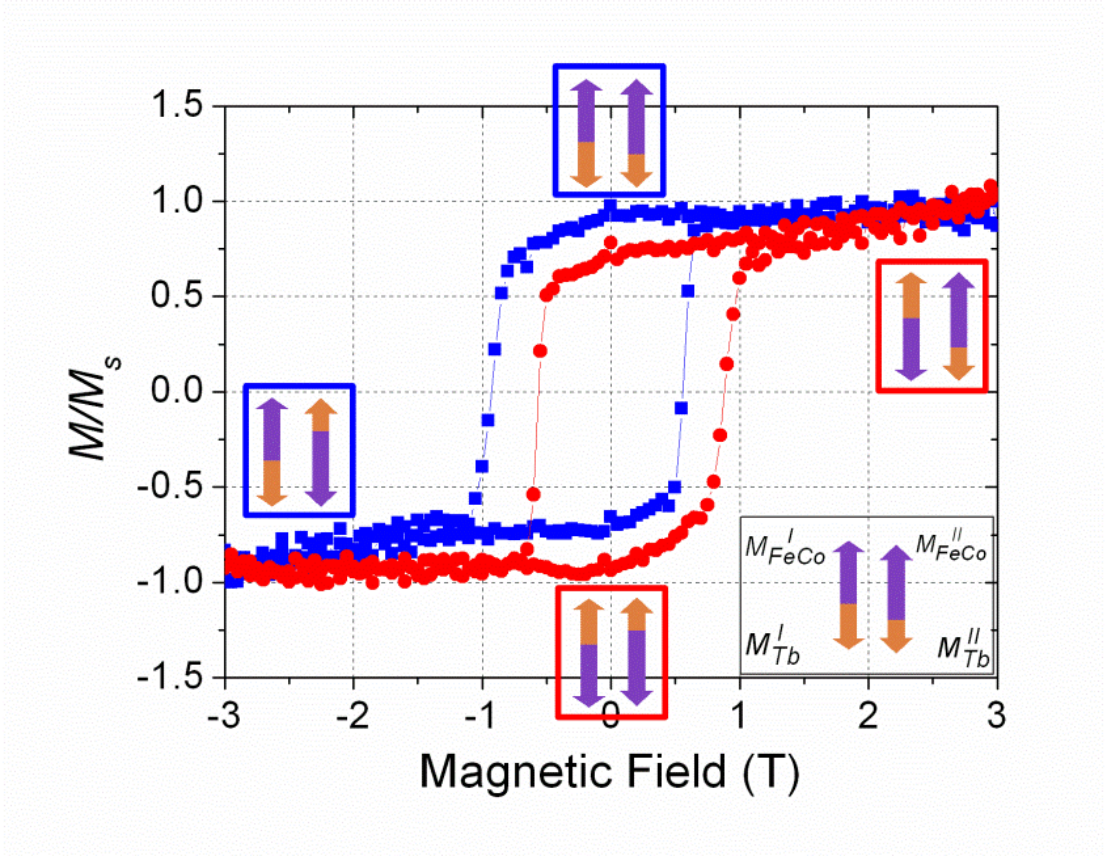

Fig. 4.2 Experimental exchange bias minor loops of TbFeCo above $T_{comp.}$ Sample initialized under 355K and 3T (blue line), and 175K and 3T (red line).

4.2.2 Below the compensation temperature

The exchange bias effect is also observed below T_{comp}. Figure 4.3 shows hysteresis loops of TbSmFeCo below T_{comp} of Phase I. At 300 K, applying an external field from 3 T through -1 T to 3 T results in positive exchange bias. Below T_{comp} of Phase I, RE moments of Phase I dominate. At 300 K and 3 T, the FeCo moments of Phase I align in the negative direction, opposite to the applied field and the FeCo moments of Phase II. At -1 T, since coercivity of Phase I am larger than 1 T, the moments of Phase I maintain their orientations. On the other hand, the moments of Phase II are reversed, and align in the same direction as those of Phase I. Since it is favorable for moments of Phase I and

Phase II to align in the same direction, a smaller external field is required to reverse the moments of Phase II when going from 3 T to -1 T, resulting in positive exchange bias. When the external field goes from -3 T through 1 T to -3 T, it results in negative exchange bias. At -3 T, the FeCo moments of Phase I align in the positive direction, while those of Phase II align in the negative direction. At 1 T, only moments of Phase II are reversed and align in the same direction as those of Phase I. Therefore, when the external field is applied from -3 T to 1 T, Phase I provides additional energy to flip the moments of Phase II, resulting in negative exchange bias.

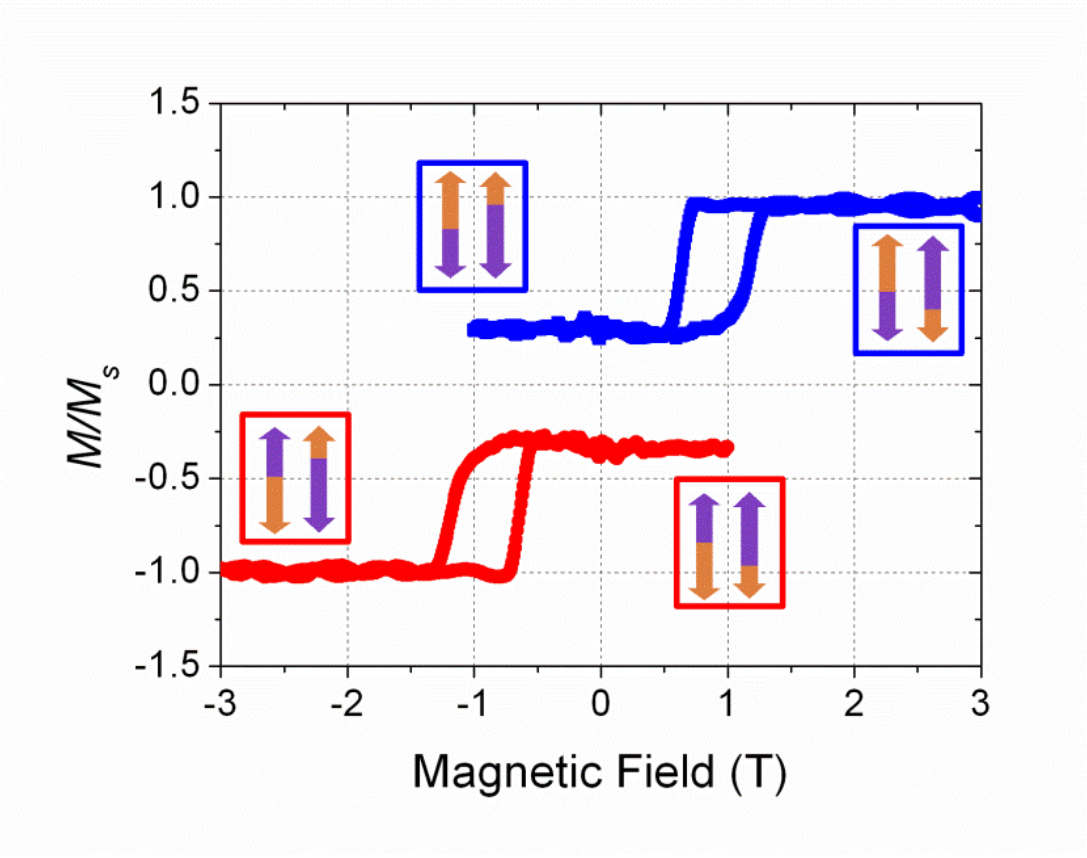

Figure 4.3 Experimental exchange bias minor loops of TbSmFeCo below $T_{comp.}$ External field scans from 3T to -1T to 3T (blue line), and from -3T to 1T to -3T (red line).

4.3 Micromagnetic Simulation with the Two-sublattice Model

In order to quantitatively validate the origin of the exchange bias effect observed in the phase-separated amorphous TbFeCo films, a two-phase model is developed [30]. Two kinds of cells, Tb-enriched and Fe-enriched, are used to represent the two nanoscale phases. A periodic boundary condition is employed. Cell sizes of 0.5 nm $\times$ 0.5 nm $\times$ 0.5 nm are employed. Local Tb-enriched (or Fe-enriched) nanophase is modeled by a cubic block containing 216 Tb-enriched (or Fe-enriched) cells. Each block is 3-nm wide, comparable to the ~2-5-nm nanophases observed in the experiment. There are 13 Phase I and 14 Phase II blocks to maintain the correct average composition. To capture the amorphous nature of the TbFeCo films, these blocks are distributed randomly in the cubic modeling space. It should be noted that in this simulation, there are two distinct compositions for each phase. In reality, there are variations in compositions for each phase, and the boundaries between the two phases are more gradual than the shape transitions employed in this simulation. The magnetic parameters of each type of cell are shown in Table 4.1. These parameters are derived from equations in section 3.2.3 using exchange constants reported by Hansen et al. [6]. The anisotropy axis of each cell is distributed within a 45-degree cone, which is consistent with the amorphous nature of TbFeCo. Since we are only interested in static behavior, we set the effective damping constant $\alpha_{\mathrm{eff}} = 1$. An external magnetic field $\boldsymbol{H}_{\mathrm{ext}}$ is applied along the axis of the anisotropy cone to study the hysteresis loops of this two-phase system. Figure 4.4 shows the temperature dependence of saturated magnetization (M_{s}) of simulated TbFeCo using the two-phase model, verifying $T_{\mathrm{comp}}$of the whole system is near 250 K, comparable to

the experimental result in Figure 4.1. In the simulations, exchange effects are observed both above and below T_{comp} and discussed in the following sections.

	Type 1	Type 2
$K_{Tb}(J/m^3)$	3.4×10^{5}	1.9×10^{5}
$A_{Tb-Tb}\ (J/m)$	1.90×10^{-12}	1.21×10^{-12}
$A_{Tb-Fe}\ (J/m)$	-2.43×10^{-12}	-1.87×10^{-12}
$A_{Fe-Fe}\ (J/m)$	1.40×10^{-11}	1.68×10^{-11}
$B_{Tb-Fe}\ (J/m^3)$	-1.43×10^{7}	-1.09×10^{7}

Table 4.1 Magnetic anisotropy constant and exchange constants of each type block used in the simulation

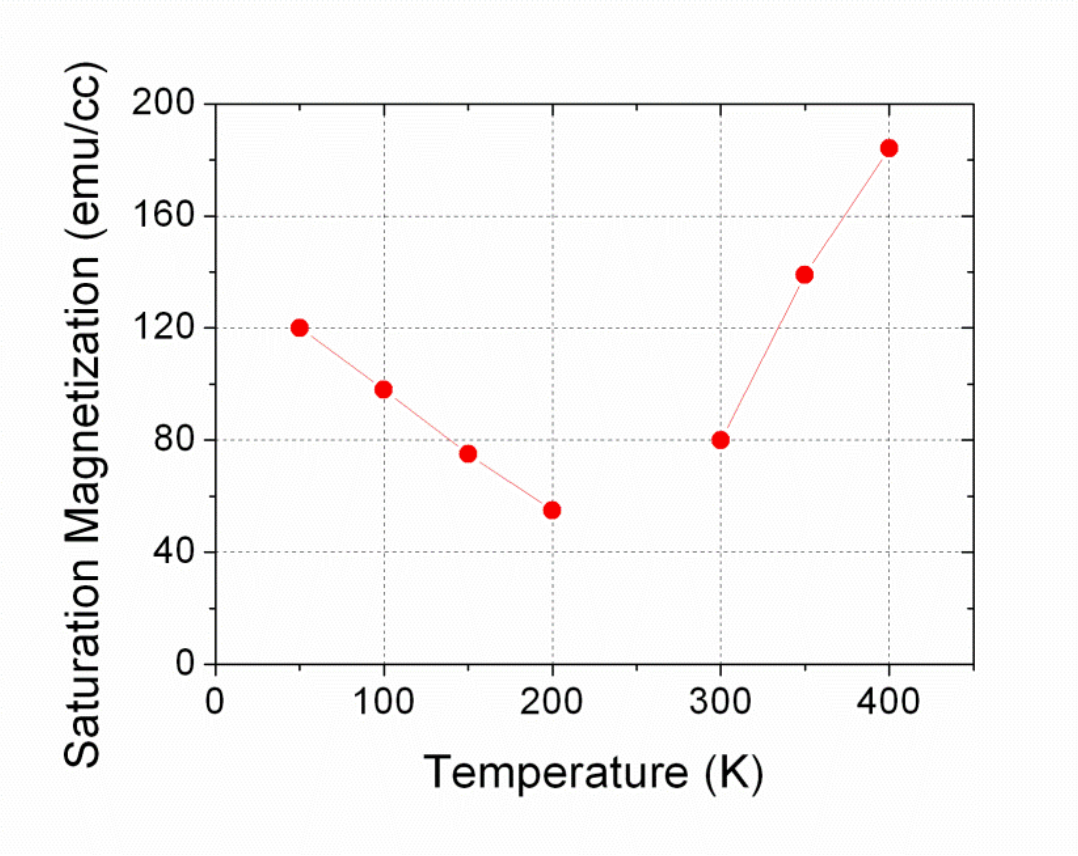

Figure 4.4 Temperature dependence of saturation magnetization simulated TbFeCo using the two-phase model.

4.3.1 Above the compensation temperature

First, the exchange bias effect is observed above T_{comp}. Figure 4.5 shows the computed hysteresis loops at 300 K. In Figure 4.5 (a), with sufficient field, moments of Phase I and Phase II are able to reverse and result in a symmetric major loop. Figure 4.5 (b) and (c) show the contribution to the major loop from each phase. Clearly, Phase I has a larger coercivity than Phase II. Figure 4.5 (d) shows exchange bias minor loops above T_{comp}. Applying an external field from 5T through -1.1 T to 5T results in a negative exchange bias minor loop. This is analogous to initialize the sample at 350 K and 3 T, then cool down to 300 K and measure the hysteresis loop in the experiment. More specifically, at 5 T external field, the FeCo moments of both Phase I and Phase II are aligned in the positive direction, in parallel to the external field, same as the spin configuration at 350 K and 3 T in the experiment. At -1.1T external field, since Phase I has coercivity larger than 1.1 T, only the moments of Phase II are reversed. Similarly, in the experiment, at 300 K, the coercivity of Phase I is larger than 3 T, so only the moments of Phase II are reversed. Therefore, applying an external field from 5 T through -1.1 T to 5 T leads to negative exchange bias minor loops, in agreement with the experiment. Positive exchange bias minor loop is observed by applying external field from -5 T through 1.1 T to -5 T. This is analogous to initialize sample at 175 K and 3 T, then warm up to 300 K to measure hysteresis loop, resulting in positive exchange bias. The shift in the hysteresis loops along the field axis ($|H_E|$) is ~0.4 T. From Figure 4.2, $|H_E|$ is ~0.3 T in the experiment. They are in excellent agreement. Using the same initial spin configurations as the experiment, this two-phase model obtains both positive and negative exchange bias minor loops, and $|H_E|$ in agreement with the experiment. Therefore, this two-phase model confirms that the

exchange coupling between the two phases observed in TbFeCo is the origin of the exchange bias effect in this system. In addition to this 3-nm two-phase model, smaller sizes of nanoscale phase separations have been used to investigate the limit of these exchange bias effects. Exchange bias effects are observed in phase separation down to 1.5nm. However, due to the limit of the micromagnetic model, where continuum approximation becomes questionable. Further numerical calculations using the atomistic model are needed to determine the phase separation size of which exchange bias effect vanishes.

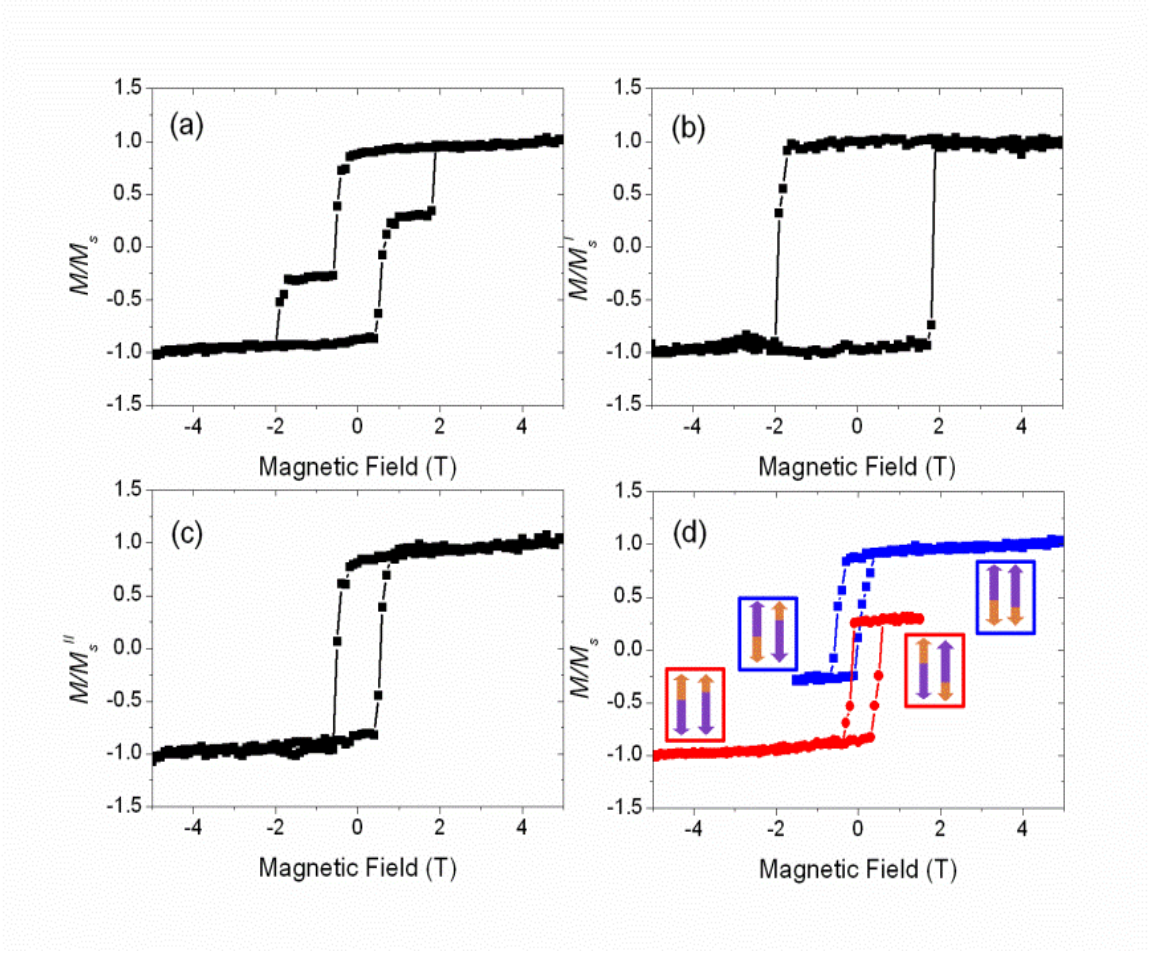

Figure 4.5 Simulated hysteresis loops of the two-phase model. (a) Major loop of TbFeCo above T_{comp}, external field scans from 5 T to -5 T to 5 T. (b-c) Contribution to the major

loop from Phase I (b) and Phase II (c) above T_{comp}. (d) Exchange bias minor loops of TbFeCo above T_{comp}. External field scans from 5 T to -1.1 T to 5 T (blue square), and from -5 T to 1.1 T to 5 T (red circle). The arrows are defined similarly as **Figure 4.1**

4.3.2 Below the compensation temperature

The exchange bias effect is also observed below T_{comp}. Figure 4.6 shows the exchange bias minor loops of TbFeCo at 200 K, below T_{comp} of Phase I. Both positive and negative exchange bias is observed. Positive exchange bias is obtained when an external field is applied from 5T through -3T to 5T. On the other hand, negative exchange bias is obtained when an external field is applied from -5T through 3T to -5T. Compare to the exchange bias effect above T_{comp}; the signs of exchange bias correspond to opposite initial spin configurations. This is due to the fact that Phase I is below T_{comp}, but Phase II is above T_{comp}. Since Phase I is below T_{comp}, the Tb moments dominate. In a sufficiently high field, the FeCo moments of Phase I align antiparallel to the external field while the FeCo moments of Phase II align parallel to the external field. As a result, Phase I provides additional exchange anisotropic energy to favor the magnetic reversal of Phase II going from 5 T to -3 T but introduces additional barrier going from -3 T to 5 T, resulting in positive exchange bias effect. The negative exchange bias effect can be understood similarly. $|H_E|$ is ~1.4 T, compared to the experimental value ~0.9 T, as shown in Figure 4.3. The difference in $|H_E|$ is due to the fact that for simplicity, Sm has not been taken into account in the numerical calculation. Since Sm has low Neel temperature, it is approximately grouped into the same sublattice as Tb in the two-phase model. Comparing to TbSmFeCo, TbFeCo has larger perpendicular magnetic anisotropy, result in a larger coercivity seen in the simulation. Therefore, with this micromagnetic model, the exchange bias effect is obtained for both above and below T_{comp}.

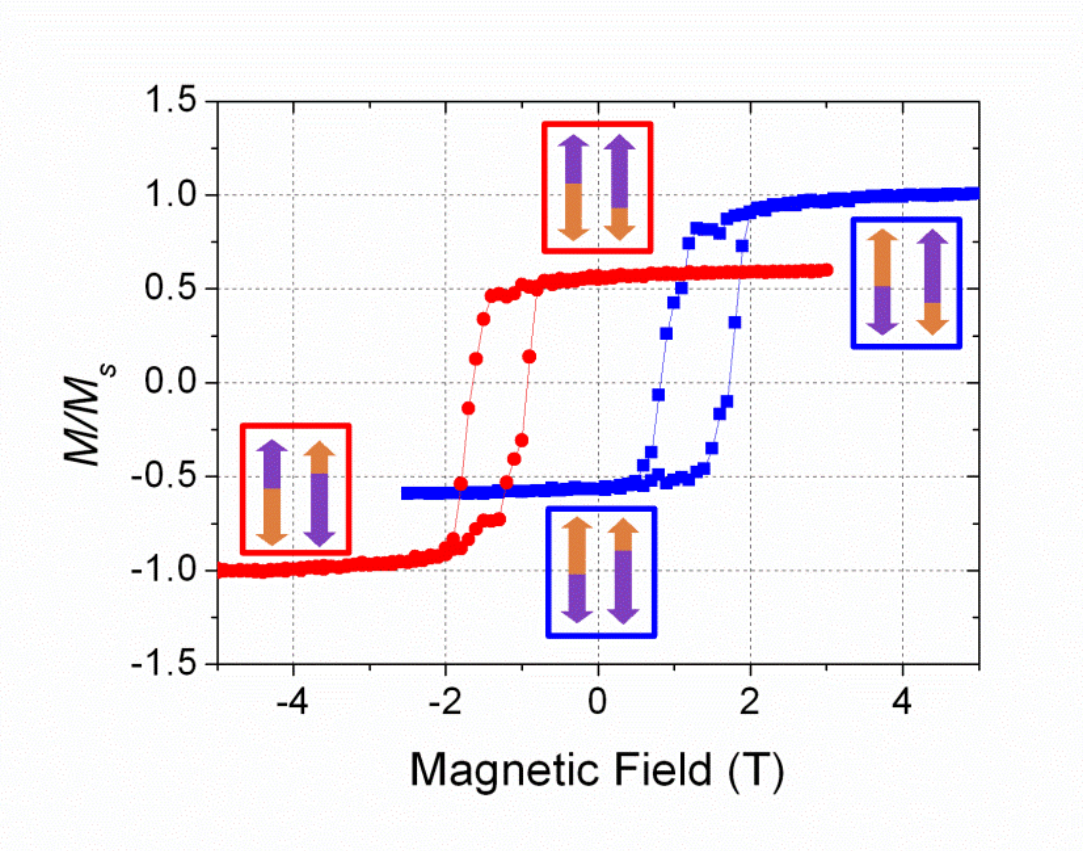

Figure 4.6 Simulated exchange bias minor loops of TbFeCo below T_{comp}. External field scans from 5 T through -3 T to 5 T (blue square), and from -5 T through 3T to -5 T (red circle). The arrows are defined similarly to Figure 4.1.

4.4 Summary and applications of the two-phase model

The micromagnetic model is employed to simulate the exchange bias effect in FiM TbFeCo films containing two nanoscale phases. The original model is extended to allow the magnetic moments of each sublattice to evolve individually. Two types of cells and blocks with distinct Tb concentrations are developed in order to incorporate the two nanoscale phases. 8 Phase I blocks and 19 Phase II blocks are randomly distributed in a 3 $\times$ 3 $\times$ 3 cube to model a structure with the two nanoscale phases. This model verifies that the observed exchange bias effect in this FiM TbFeCo films originates from the exchange

interaction between the two nanoscale phases. Moreover, both positive and negative exchange bias loops have been observed above and below T_{comp}, and the signs of the exchange bias effect are in agreement with the experimental results. Using this micromagnetic model, one can explore FiM/FM and FiM/FiM systems by tuning the composition of the nearly compensated FiM phase, and develop desirable exchange bias properties for applications at room temperature.

In addition to understand the exchange bias effect in a two-phase RE-TM system, this micromagnetic model can also be employed to study exchange bias effects in other two-phase materials with FiM phase. For example, intrinsic exchange bias effects have been reported in polycrystalline Heusler alloys at low temperature [41-42]. An exchange field of more than 3T is uncovered in Mn-Pt-Ga with the coexistence of FM and FiM regions and shows a strong dependence on compositions and field-cooled procedures [42]. The two-phase model can be employed to study this tunable exchange bias effect in Mn-Pt-Ga. With different compositions of the FiM phase and initialization conditions, one can understand how they contribute to the tunable exchange bias effect and lead to the development of new two-phase exchange bias materials using FiM to achieve desirable properties for applications.

5. Control of Anisotropy in TbFeCo Thin Films through Strain Effect

5.1 Introduction

The metal-insulator transition (MIT) of vanadium dioxide (VO_2) has drawn interest from both fundamental theories and technological applications [51, 52]. Recent studies have shown possible applications in ultrafast optics and electronic devices for sensing and switching [53-57]. In bulk VO_2, MIT at ~340K [58] is accompanied by an abrupt change in structure and electronic properties. Across MIT, VO_2 undergoes a structural transition from low-temperature monoclinic to high-temperature rutile phase. In VO_2 thin films under uniaxial strain, recent reports reveal a complex mix of structural phases near MIT [59-63]. In a similar V_2O_3 system, this coexistence of nanoscale phases near MIT leads to changes in magnetic properties in V_2O_3/Ni bilayers [64, 65]. Moreover, magnetism in paramagnetic centers is found to be affected by MIT in VO_2 due to magnetoelastic anisotropy [66]. In these samples, the strain effect that arises from MIT serves as the most important mechanism on tuning magnetic properties. Because of their high magnetostrictions, ferrimagnetic rare-earth (RE) transitional-metal (TM) alloys such as TbFeCo are promising materials to study the effect on magnetism from MIT. In addition to large magnetostrictions, the flexibility and tunability of amorphous RM-TM films make them good materials to employ to reveal the effect on magnetism from MIT.

In this chapter, the tuning of magnetic properties in amorphous TbFeCo through interfacial strain from the bending of the Kapton substrate is first investigated. This sets the benchmark for magnetostrictions of TbFeCo thin films. Then, amorphous TbFeCo deposited on epitaxial VO_2 is studied. A reference sample was prepared on Si/SiO_2 substrate. A comparison of magnetic properties demonstrated the changes in magnetic

anisotropy and magnetization in TbFeCo near MIT of VO_2. Furthermore, we determined the magnitude of the strain exerted on TbFeCo in the heterostructures. The results provided a better understanding of developing techniques to control magnetic properties through MIT for device applications.

5.2 Substrate-bending Experiment with Kapton Substrate

The magnetostriction of amorphous TbFeCo was measured through the substrate bending experiment. A 100 nm TbFeCo sample was deposited on flat 125μm thick 100HN a Kapton® substrate. Figure 5.1 shows the substrate bending configuration with the Kapton substrate. From left to right, the sample is flat (relax), under convex bending (tension), and concave bending (compression). Using the Van der Pauw method [17] described in section 2.3.2, the Hall Effect is measured, and the out-of-plane coercivity from 200 K to 300 K is shown in Figure 5.2. Results show that the sample under tension has smaller coercivity (6500 Oe at 300 K) than sample under compression (9000 Oe at 300 K). This is consistent with the fact that tensile stress introduces negative anisotropy in TbFeCo (positive magnetostriction) sample, while compressive stress introduces positive anisotropy.

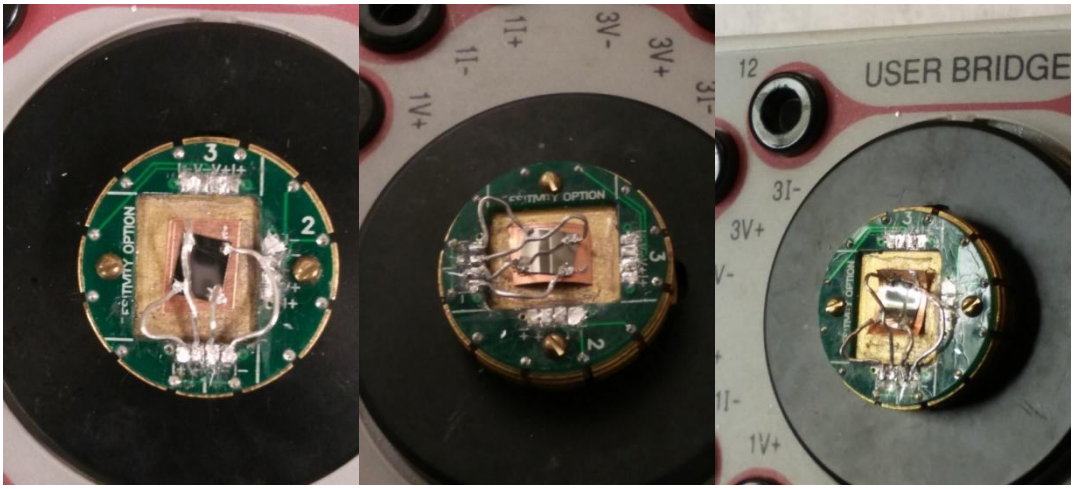

Figure 5.1 Substrate bending configuration with a Kapton substrate. From left to right, flat, convex bending (tension), concave bending (compression)

However, the sample under compression has a smaller coercivity than the flat sample (10500 Oe at 300 K), which contradicts the expectation. This is likely due to the fact that when the sample is under bending, not all the sample is perpendicular to the applied field, and the applied field is at an angle to the easy axis and a smaller coercivity.

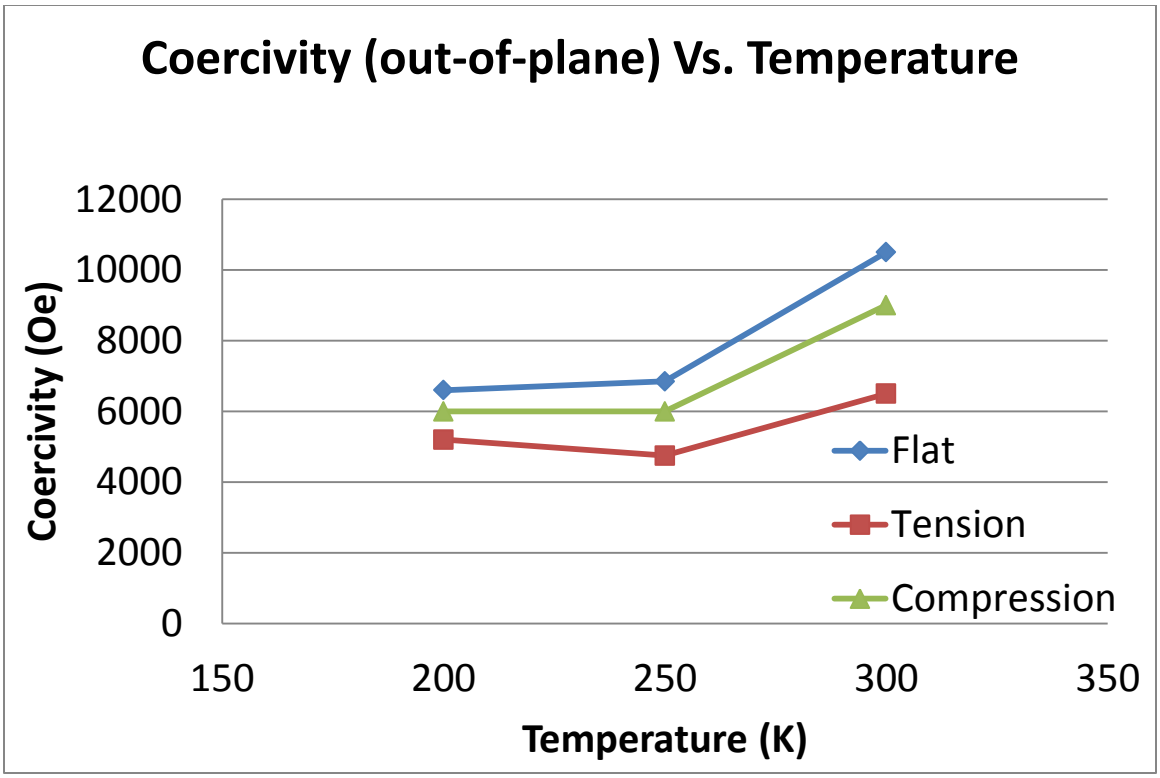

Figure 5.2 Coercivity (out-of-plane) Vs. Temperature, for flat, convex bending (tension), concave bending (compression)

Figure 5.3 shows the measured hysteresis loops at 200 K through Hall effect measurement. The squareness (M_R/M_S) of the hysteresis loop, which is defined as the remanent magnetization M_R divided by the saturation magnetization M_s, are different for tension (~0.8), flat (~0.95) and compression (~1). This indicates that applying stress can change the anisotropy in the sample. Applying compressive stress introduces positive anisotropy and leads to an "easier" axis in the perpendicular direction. On the other hand, applying tensile stress introduces negative anisotropy and leads to a "harder"-axis in the perpendicular direction.

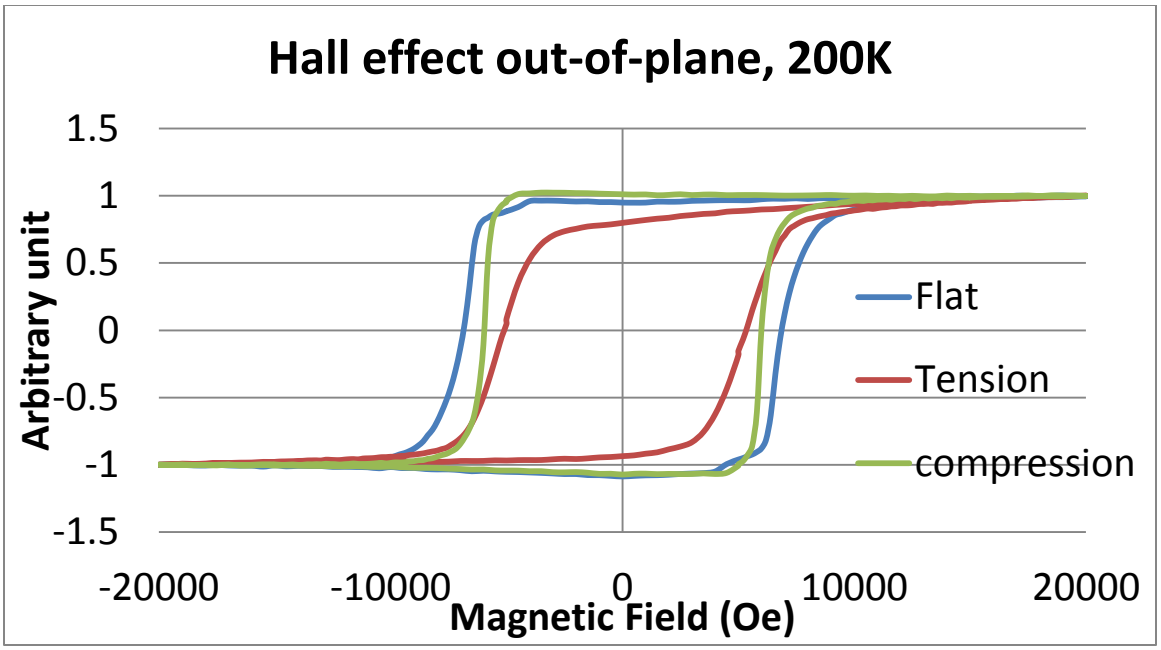

Figure 5.3 Out-of-plane hysteresis loop Vs. Temperature, for flat, convex bending (tension), concave bending (compression) at 200 K.

To quantitatively measure the changes in anisotropy, in-plane measurement is needed to determine the anisotropy field. Using VSM, the substrate is bent at various degrees, from tension to flat to compression. Figure 5.4 summarizes the in-plane anisotropy field at 300 K. Results show that anisotropy decreases as applied stress increases. This can be explained by the following equation for anisotropy K_u.

$$K_u = -K_0 \cos^2\theta - K_{ap}\cos^2\theta_{ap} = -K_0\cos^2\theta + \frac{3}{2}\lambda_s\sigma_{ap}\cos^2\theta_{ap}$$

where λ_s is the saturation magnetostriction of the sample, and θ_{ap} is the angle between the magnetic moment in the sample and the perpendicular direction to the applied stress.

In a positive magnetostrictive material, when compression is applied ($\sigma_{ap} < 0$), the spins would prefer to align in the out-of-plane direction, resulting in stronger perpendicular magnetic anisotropy. When tension is applied($\sigma_{ap} > 0$), it is more favorable for in-plane

alignment, leading to weaker perpendicular magnetic anisotropy. Using a linear fit of $H_k \; vs. \; \sigma_{ap}$, the slope is $-1.0 \pm 0.1 \text{kOe/GPa}$. The saturation magnetostriction $\lambda_s$is derived according to [67, 68]

$$\lambda_s = \frac{\mu_0 M_s}{3} \frac{H_K}{\sigma_{ap}} \qquad (3)$$

This gives saturation magnetostriction λ_s of $(42 \pm 4) \times 10^{-6}$.

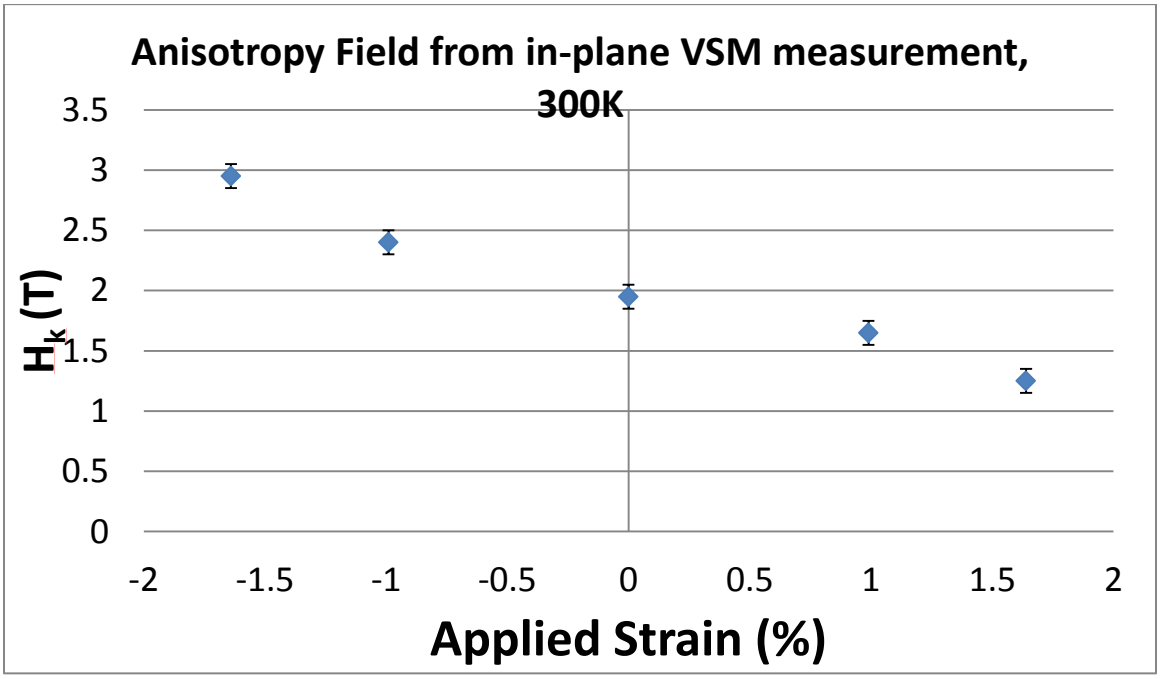

Figure 5.4 In-plane anisotropy field vs. applied strain at 300K. Same sample was used for all the measurements.

5.3 Strain Effect through Metal-insulator Transition in VO_2/TbFeCo

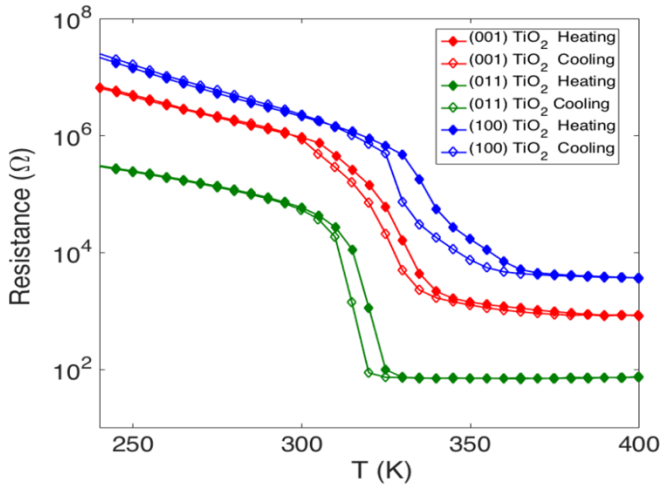

Figure 5.5 Resistance obtained from 240K to 400K in VO_2 on TiO_2 (011) (green), VO_2 onTiO_2 (001) (red) and VO_2 onTiO_2 (100) (blue). MITs of different orientations are observed at different temperatures between 310K and 350K.

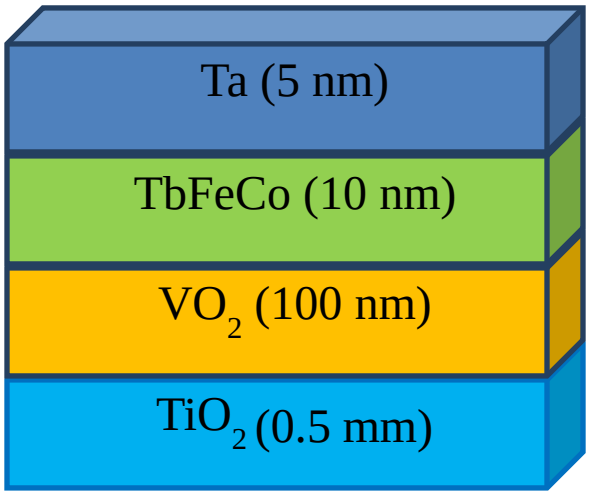

Figure 5.6 An illustration of the VO_2/TbFeCo heterostructure (not to scale).

To study strain effect through MIT in VO_2/TbFeCo heterostructure, ~100 nm VO_2 thin films were grown on (011), (001), and (100) TiO_2 substrates by Prof. Jiwei Lu's group using reactive biased target ion beam deposition (RBTIBD) [69]. Figure 5.5 shows the resistance measurement of VO_2 with various orientations, obtained by Dr. Yuhan Wang.

Results show that MIT of VO2 on TiO_2 (011), VO_2 onTiO_2 (001), and VO_2 onTiO_2 (100) are 320 K, 335K and 350 K respectively. 15 nm Amorphous $Tb_{26}Fe_{64}Co_{10}$ thin films were deposited on VO_2/TiO_2 films and thermally oxidized Si substrates by RF magnetron sputtering at room temperature under base pressure of 5×10^{-7} torr from co-sputtering of Tb and TbFeCo targets. The TbFeCo layers were deposited on the VO_2/TiO_2 films and SiO_2/Si substrates at the same time to eliminate changes in TbFeCo properties due to growth conditions. A 5 nm Ta capping layer was deposited on the samples to prevent oxidation. Figure 5.6 shows an illustration of the VO_2/TbFeCo heterostructure. These samples were made in Hall bar devices for magneto-transport measurement [70]. During Hall bar fabrication, the TiO_2 (001)/ VO_2/TbFeCo heterostructure sample was destroyed. Thus, magneto-transport measurements were only obtained for TiO_2 (100)/VO_2/TbFeCo, TiO_2 (110)/VO_2/TbFeCo, and Si/SiO_2/TbFeCo samples.

To determine the strain effect of VO_2 on TbFeCo, Hall effect measurements of TiO_2 (100)/VO_2/TbFeCo, TiO_2 (110)/VO_2/TbFeCo are compared to the Si/SiO_2/TbFeCo standard sample. Figure 5.7 presents the Hall effect results of TbFeCo on SiO_2/Si and VO_2/TiO_2. In Figure 5.7(a) Hall measurement of Si/SiO_2/TbFeCo sample shows no changes to hysteresis loops from 310K to 335K. This result is expected because the SiO_2/Si substrate does not undergo a phase transition between 310K and 335K. This result also verifies that the magnetic properties of TbFeCo are robust between 310K and 335K. Figure 5.7(b) shows the Hall results of TiO_2 (110)/VO_2/TbFeCo from 310K to 320K. As temperature approaches MIT of VO_2 on TiO_2 (011), 320K, the hysteresis loops of TbFeCo become less squared. This corresponds to a decrease in perpendicular magnetic anisotropy. Since no changes in observed in the standard sample

Si/SiO_2/TbFeCo, the decrease in perpendicular magnetic anisotropy is due to the MIT of VO_2 on TiO_2(011). Similar behavior is also observed in TiO_2 (100)/VO_2/TbFeCo, as shown in Figure 5.7(c). The hysteresis loops are less squared and provide evidence of a decrease in perpendicular magnetic anisotropy.

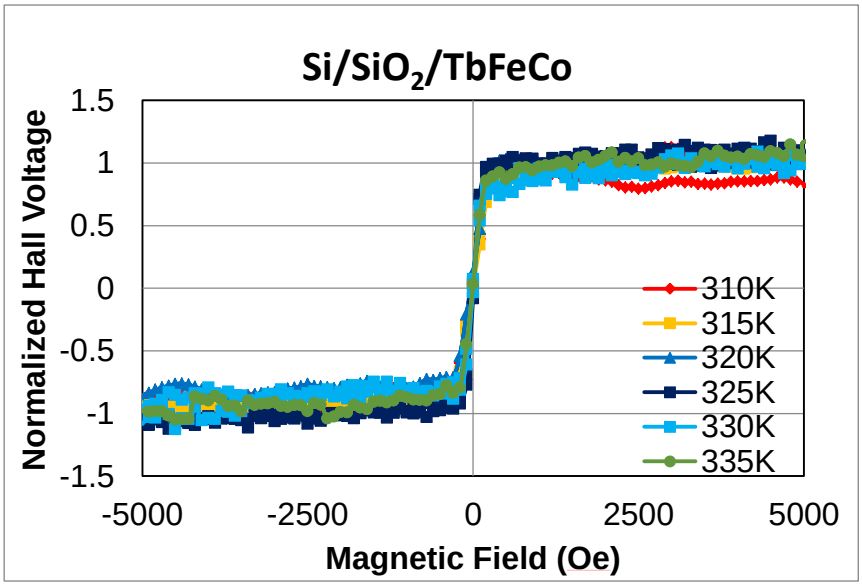

(a)

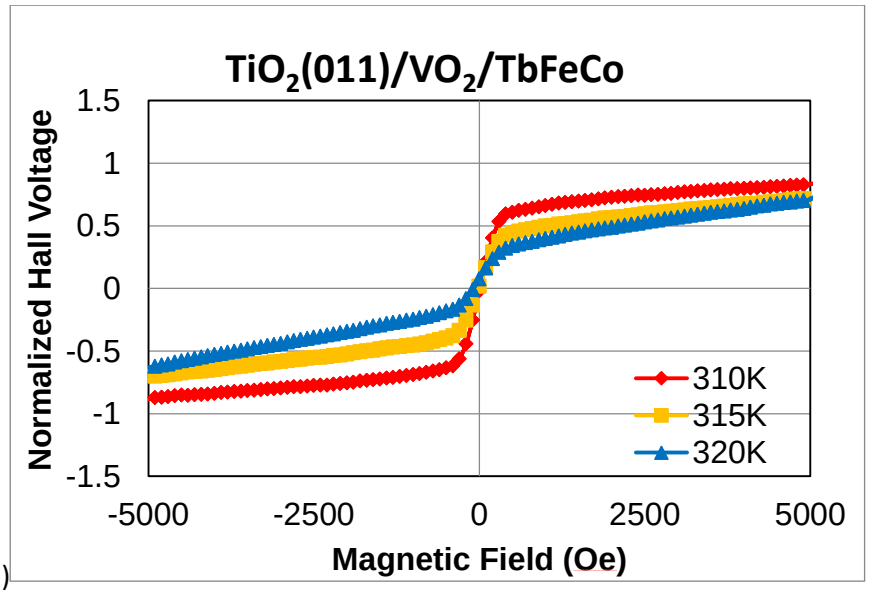

(b)

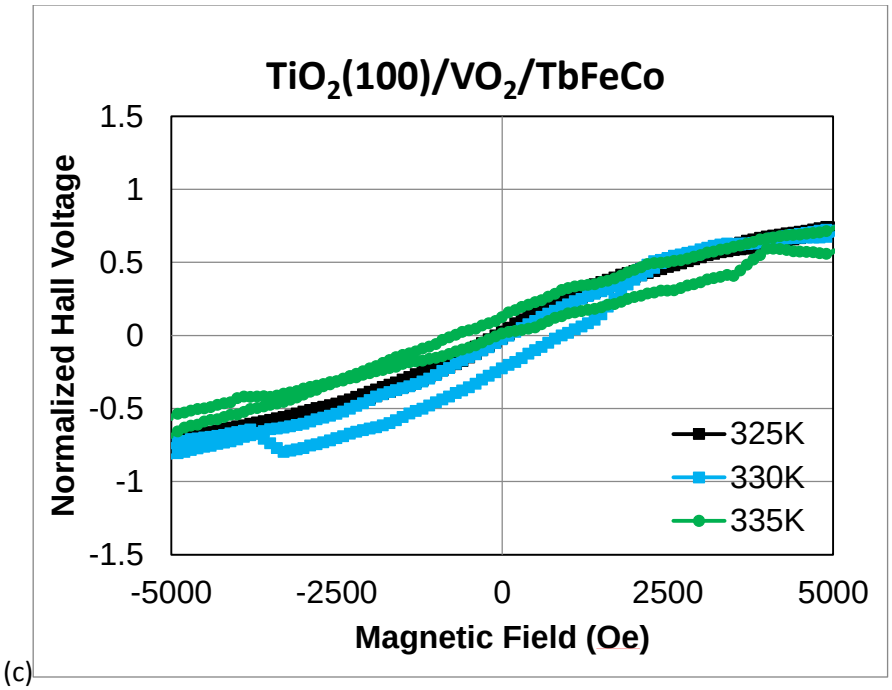

(c)

Fig. 5.7 Anomalous Hall effect of TbFeCo measured at various temperatures. (a) $Si/SiO_2/TbFeCo$; (b) TiO_2 (011)/VO_2/TbFeCo; (c) TiO_2 (100)/VO_2/TbFeCo.

Temperature (K)	$Si/SiO_2/TbFeCo$	$TiO_2(011)/VO_2/TbFeCo$	$TiO_2(100)/VO_2/TbFeCo$
310	0.22	0.12	
315	0.17	0.07	
320	0.24	0.01	
325	0.37		0.03
330	0.33		0.02
335	0.29		0.01

Table 5.1 Summary of TbFeCo the squareness (M_r/M_s) at various temperatures for $Si/SiO_2/TbFeCo$, TiO_2 (011)/VO_2/TbFeCo, and TiO_2 (100)/VO_2/TbFeCo.

Table 5.1 summarizes the squareness (M_r/M_s) of out-of-plane hysteresis loops in $Si/SiO_2/TbFeCo$, TiO_2 (011)/VO_2/TbFeCo, and TiO_2 (100)/VO_2/TbFeCo. In $Si/SiO_2/TbFeCo$, the squareness remains around 0.3 from 310 K to 335 K. This result points to little or no changes in magnetic anisotropy in TbFeCo samples on a regular substrate. For TbFeCo on VO_2, the squareness decreases to 0.01as VO_2 undergoes structural transition. In $TiO_2(011)/VO_2/TbFeCo$, the squareness decreases from 0.12 at

310 K to 0.01 at 320 K as temperature crosses the MIT of VO_2 on TiO_2(011) at 320 K. Similarly, in TiO_2(100)/VO_2/TbFeCo, the squareness decreases from 0.03 at 325 K to 0.01 at 335 K as temperature crosses the MIT of VO_2 on TiO_2(011) at 335 K. These decreases in squareness verify the decrease in magnetic anisotropy in TbFeCo due to stress originated from the structural transition of VO_2.

Stress arises from phase transition of VO_2 near MIT is likely the cause of the changes in anisotropy of TbFeCo. The change in anisotropy energy ΔK_u due to applied stress from VO_2 MIT is given by the following.

$$\Delta K_u = -\frac{3}{2}\lambda_s \sigma_{ap} \cos^2 \theta_{ap}$$

Since saturation magnetostriction λ_s of TbFeCo is positive, a decrease in perpendicular magnetic anisotropy corresponds to positive stress on TbFeCo due to VO_2 structural transition. Therefore, the stress from VO_2 transitioning from an insulating state to a metallic state is tensile.

To estimate the applied stress on TbFeCo from VO_2 structural transition, micromagnetic model is employed to study the change in anisotropy energy. Using OOMMF [27] and an effective ferromagnetic model for a ferrimagnetic film [71], hysteresis loops are simulated and compared to experiment. The following parameters are used in the simulation: cell size of 3 nm, $M_s = 1 \times 10^5 A/m$, $A = 1.5 \times 10^{-11} J/m$, and a variable K_u with a 45-degree cone to model the change in anisotropy due VO_2 structural transition.

Figure 5.8 shows the results of hysteresis loops with different anisotropy energy K_u. As shown in Figure 5.8, the small but squared hysteresis loops in Si/SiO_2/TbFeCo standard

sample corresponds to the hysteresis loop of $K_u = 1.5 \times 10^3 J/m^3$. The hysteresis loops become less squared at $K_u = 1 \times 10^3 J/m^3$, which corresponds to the changes observed in the TiO_2 (011)/VO2/TbFeCo sample. The change is anisotropy energy ΔK_u is estimated to be $-1 \times 10^3 J/m^3$ and the tensile stress on TbFeCo due to VO_2 on TiO_2 (011) structural transition is estimated to be about 8 MPa. For the TiO_2 (100)/VO_2/TbFeCo sample, the change in squareness is more pronounced. The tensile stress on TbFeCo due to VO_2 on TiO_2 (100) transition is in more than 8 MPa. It is also possible to introduce compressive strain from VO_2 by tuning the MIT such that VO_2 is transitioning from metallic state to insulating state. This opens up a new method to control magnetostrictive materials, such as amorphous TbFeCo, through MIT for desirable applications.

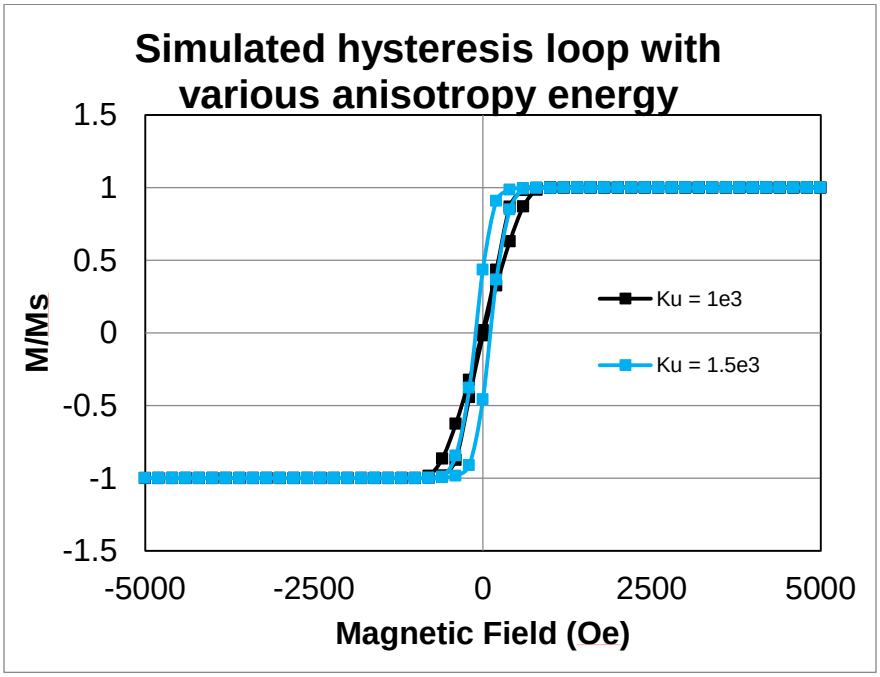

Figure 5.8 Simulated out-of-plane hysteresis loops with various anisotropy energy K_U.

5.4 Summary

Tuning of magnetic anisotropy through the interfacial strain was investigated in TbFeCo on Kapton substrate and on VO_2 epitaxially grown on a TiO_2 substrate. In the substrate bending experiment with Kapton, tensile and compressive stress was found to decrease and increase perpendicular magnetic anisotropy in TbFeCo, respectively. The magnetostriction of TbFeCo is found to be $(42 \pm 4) \times 10^{-6}$. In VO_2/TbFeCo heterostructure, through the structural transition at MIT, VO_2 applies tensile strain on TbFeCo. Results show that a decrease in squareness in out-of-plane hysteresis loops. Through micromagnetic simulation, a tensile strain of about 8 MPa is applied by the underlying VO_2 layer across MIT. These results show the potential to control the magnetic anisotropy of TbFeCo through MIT of VO_2. In magnetic memory devices, the capability to control magnetic anisotropy can provide flexibility in writing and storing information using TbFeCo.

6. Atomistic Modeling of Skyrmions

6.1 Introduction

Magnetic skyrmions are magnetic spin textures that have the potential to advance energy density and efficiency in magnetic memory devices [72-77]. In magnetic materials, skyrmions are stabilized through the Dzyaloshinskii Moriya interaction (DMI) [78, 79], generated by symmetry breaking from intrinsic or interfacial asymmetries. Bloch skyrmions are formed in non-centrosymmetric B20 alloys such as MnSi and CoGe below room temperature [80, 81]. On the other hand, interfacial DMI originates from a heavy metal interface is found to stabilize skyrmion in ferromagnet [82, 83] and amorphous ferrimagnet at room temperature. Large skyrmions of ~150 nm have been observed in Pt/GdCo/MgO [84], and small skyrmions close to 10 nm were found in Pt/GdCo/TaO_x [16] thin films. Challenge remains to optimize skyrmions for room temperature applications. Further reduction in skyrmion size and increase stability is required for device applications.

In this chapter, numerical simulation is employed to guide experimental works in obtaining sub 10 nm skyrmions at room temperature. An atomistic LLG algorithm [85] is used to investigate the properties of skyrmions in GdCo with interfacial DMI. The phase space of various tunable parameters, include thickness, T_{comp}, anisotropy, and interfacial DMI, are explored to identify the optimum properties of GdCo to skyrmions at room temperature [86].

6.2 Modeling Techniques

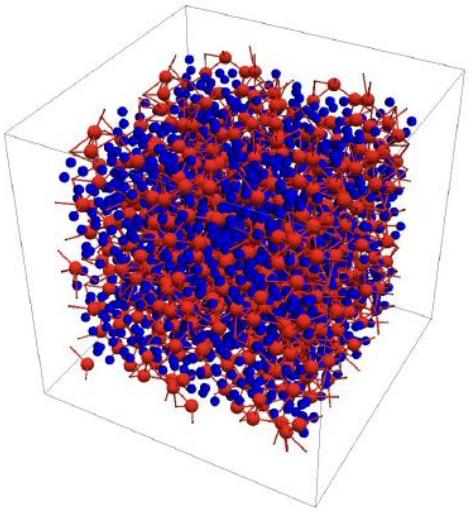

Figure 6.1 Amorphous structure of $RE_{25}TM_{75}$ from ab initio molecular dynamics calculations. Red atoms are rare-earth, and blue atoms are transition-metal.

Parameter	Value
Gyromagnetic ratio (ϒ)	2.0023193
Gilbert Damping (α)	0.05
Gd moment (μ_{Gd})	7.63 μ_B
Co moment (μ_{Co})	1.72 μ_B
Gd-Gd exchange constant ($J_{Gd\text{-}Gd}$)	1.26 x 10^{-21} J
Co-Co exchange constant ($J_{Co\text{-}Co}$)	3.82 x 10^{-21} J
Gd-Co exchange constant ($J_{Gd\text{-}Co}$)	-1.09 x 10^{-21} J

Table6.1 Values of parameters used in the simulation**.**

In this study, the atomistic model from section 3.3 is employed to calculate the effective field $\mathbf{H_{eff}}$ and the Landau-Lifshitz-Gilbert (LLG) equation is used to evolve the atomistic spins. Table 6.1 summarizes the values of parameters used in the simulations. Exchange couplings J's are calibrated based on Ostler *et al.* [87] to maintain the same Curie temperature and compensation temperature for a given composition. Anisotropy energy is

determined based on Hansen *et al.* [6]. Only nearest neighbor interactions are considered in the exchange and DMI interactions. Periodic boundary conditions are enforced in the x and y directions.

Figure 6.1 shows the amorphous structure of $RE_{25}TM_{75}$ used in this study. This structure was generated by Sheng *et al.* [88] from ab initio molecular dynamics calculations. The original amorphous structure is a 1.6 nm x 1.6 nm x 1.6 nm box containing 250 atoms. For $Gd_{25}Co_{75}$, the compensation temperature (T_{comp}) is 250 K. For this study, replicas of this box (32 x 32 x n) are placed next to each other to expand the simulated sample to 50.7 nm x 50.7 nm x (4.8 nm to 15.2 nm). The thickness in this study varies from 4.8 nm to 15.2 nm. In a sample of 50.7 nm x 50.7 nm x 4.8 nm, there is a total of 768000 atoms, and on average, each Co atom has 6.8 Co neighbors and 4.1 Gd neighbors, while each Gd atom has 11.7 Co neighbors and 3.5 Gd neighbors. The size of skyrmions is defined as the diameter for which $M_z = 0$. Since skyrmions are not perfectly symmetric, the size of a skyrmion is determined from the averaging of diameter in different directions.

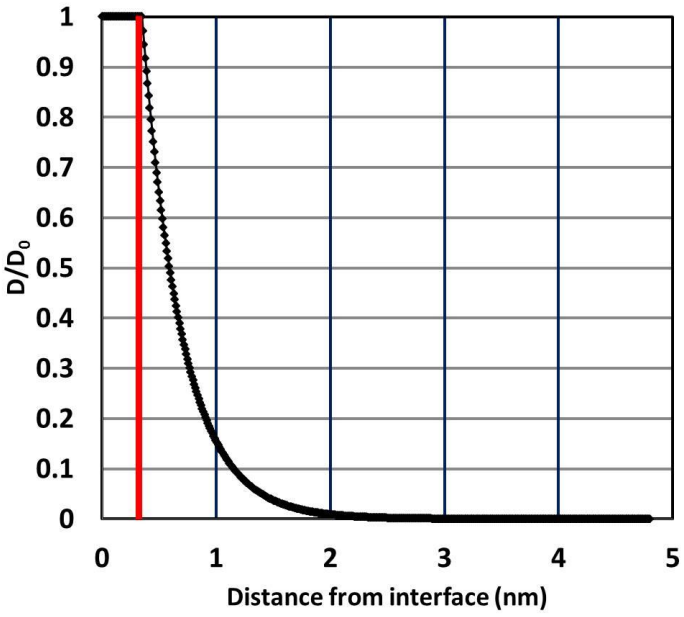

Figure 6.2 Exponential decay DMI in 5 nm GdCo as function of distance from bottom interface (z). In this model, DMI remains constant (D_0) within 0.35 nm of the bottom interface, as indicated by the red line. Away from the interface, the strength of DMI decays exponentially, as shown.

Figure 6.2 shows the functional form of DMI employed in this study. In the decaying DMI model, DMI decays exponentially, and D (z) is given by

$$\mathrm{D(z)} = D_0 \qquad \text{for z} \leq z_0$$

$$\mathrm{D(z)} = D_0 e^{-\frac{z-z_0}{\lambda}} \qquad \text{for z} > z_0$$

where D_0 is the interfacial DMI, $z_0 = 0.375$ nm, and $\lambda = 0.375$ nm are parameters of the exponential decay.

$z_0 = 0.35$ nm represents a constant DMI over the first pair nearest neighbor in the amorphous structure. $\lambda = 0.35$ nm represents the decay length of DMI, which is approximated using the following method based on the measured results of DMI.

In general, the average DMI $\mathrm{D_{ave}}$ of a sample of thickness t_s is given by

$$\mathrm{D_{ave}} = \frac{1}{t_s}\int_0^{t_s} D(z)\, dz$$

where D (z) is the DMI at distance z away from the interface.

In the decaying DMI model,

$$\mathrm{D_{ave}} = \frac{\mathrm{D_0}}{t_s}\left(z_0 + \lambda - e^{-\frac{t-z_0}{\lambda}}\right)$$

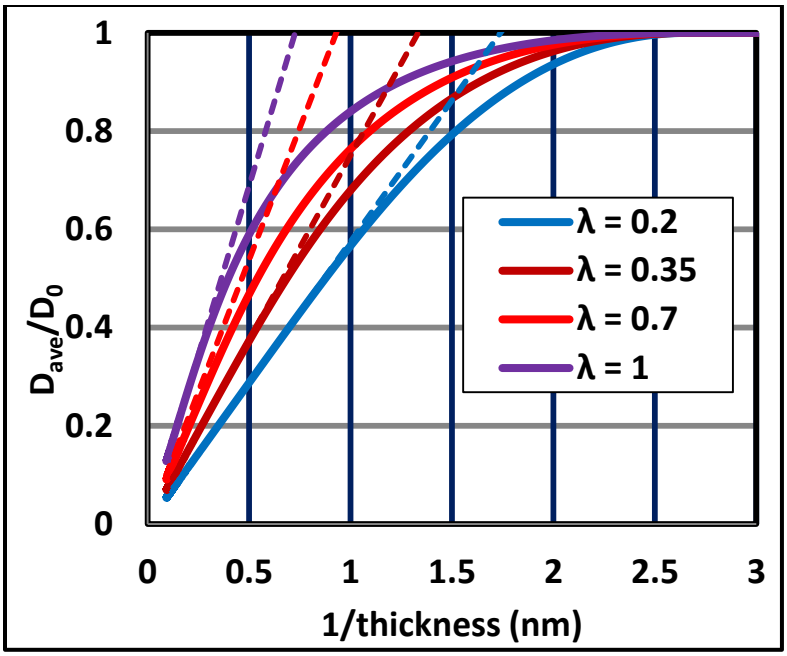

Figure 6.3 Plot of D_{ave}/ D_0 as a function of $1/t_s$. ($z_0 = 0.35\ nm$) Dashed lines represent a linear relationship between D_{ave} and $1/t_s$.

Figure 6.3 shows the plot of D_{ave}/ D_0 as a function of $1/t_s$. For different decay length λ, the derivation from $1/ t_s$.occurs at different t_s. The derivation from $1/ t_s$ can be used to approximated λ using the measured DMI in Co and ferromagnetic Co alloys with Pt interface. [89-93]

D_{ave} begins to deviate from $1/ t_s$ at $1/ t_s$ around 0.8 to 1.2 nm^{-1}, which corresponds to λ ~0.2 to 0.3 nm. This is about the first pair nearest neighbor in Co, so λ = 0.35 nm is used in this study, which corresponds to the first pair nearest neighbor in the amorphous structure.

6.3 Skyrmions in Ferrimagnetic GdCo

A range of interfacial DMI values, from $d_{Co\text{-}Co} = 0.1 \times 10^{-22}$ J to $d_{Co\text{-}Co} = 2.0 \times 10^{-22}$ J (D = 0.12 to 2.38 mJ/m^2), and three thicknesses, 5 nm, 10 nm, and 15 nm, are considered. Only

those show skyrmions are shown herein. To shorten the computational time, thicker samples of 10 nm and 15 nm are simulated using a 5 nm sample by conserving DMI energy density across the film. To check the validity of this simplification, we have compared the results of 10 nm samples and verified that the condensed 5 nm samples produce identical results. First, we consider two scenarios for the sign of $d_{Gd\text{-}Co,}$ as both + and - signs have been reported in antiferromagnetically coupled systems [94, 95]. Figure 6.4 shows the color maps of equilibrium spin configurations at 300 K for both $d_{Gd\text{-}Co} > 0$ and $d_{Gd\text{-}Co} < 0$. For the case of $d_{Gd\text{-}Gd}$, $d_{Co\text{-}Co} > 0$ and $d_{Gd\text{-}Co} > 0$, the simulation with $d_{Co\text{-}Co} = 0.25 \times 10^{-22}$ J, $d_{Gd\text{-}Gd} = 2.96 \times 10^{-22}$ J and $d_{Gd\text{-}Co} = 0.86 \times 10^{-22}$ J corresponds to an average DMI of D = 0.21 mJ/m^2. The value of $d_{Gd\text{-}Gd}$ and $d_{Gd\text{-}Co}$ is calculated from $d_{Co\text{-}Co}$ by multiplying the ratio of Gd moment μ_{Gd} over Co moment μ_{Co}. The following equation shows the formula used for converting atomistic DMI to average DMI for Gd_xCo_{1-x}.

$$D = \frac{2}{\pi}\frac{1}{\bar{n}}\left[(1-x)\left(\frac{\overline{n_{Co-Co}}d_{Co-Co}}{\overline{r_{Co-Co}}^2} + \frac{\overline{n_{Co-Gd}}|d_{Gd-Co}|}{\overline{r_{Co-Gd}}^2}\right) + x\left(\frac{\overline{n_{Gd-Gd}}d_{Gd-Gd}}{\overline{r_{Gd-Gd}}^2} + \frac{\overline{n_{Gd-Co}}|d_{Gd-Co}|}{\overline{r_{Gd-Co}}^2}\right)\right]$$

where $\bar{n}$ is the average number of nearest neighbors around all atoms, $\overline{n_{A-B}}$ is the average number of atoms A that are nearest neighbors to atom B, $\overline{r_{A-B}}$ is the average distance between atoms A and nearest neighboring atom B. The $\frac{2}{\pi}$ factor comes from averaging of the cross product $\boldsymbol{s_i} \times \boldsymbol{s_j}$ in DMI energy.

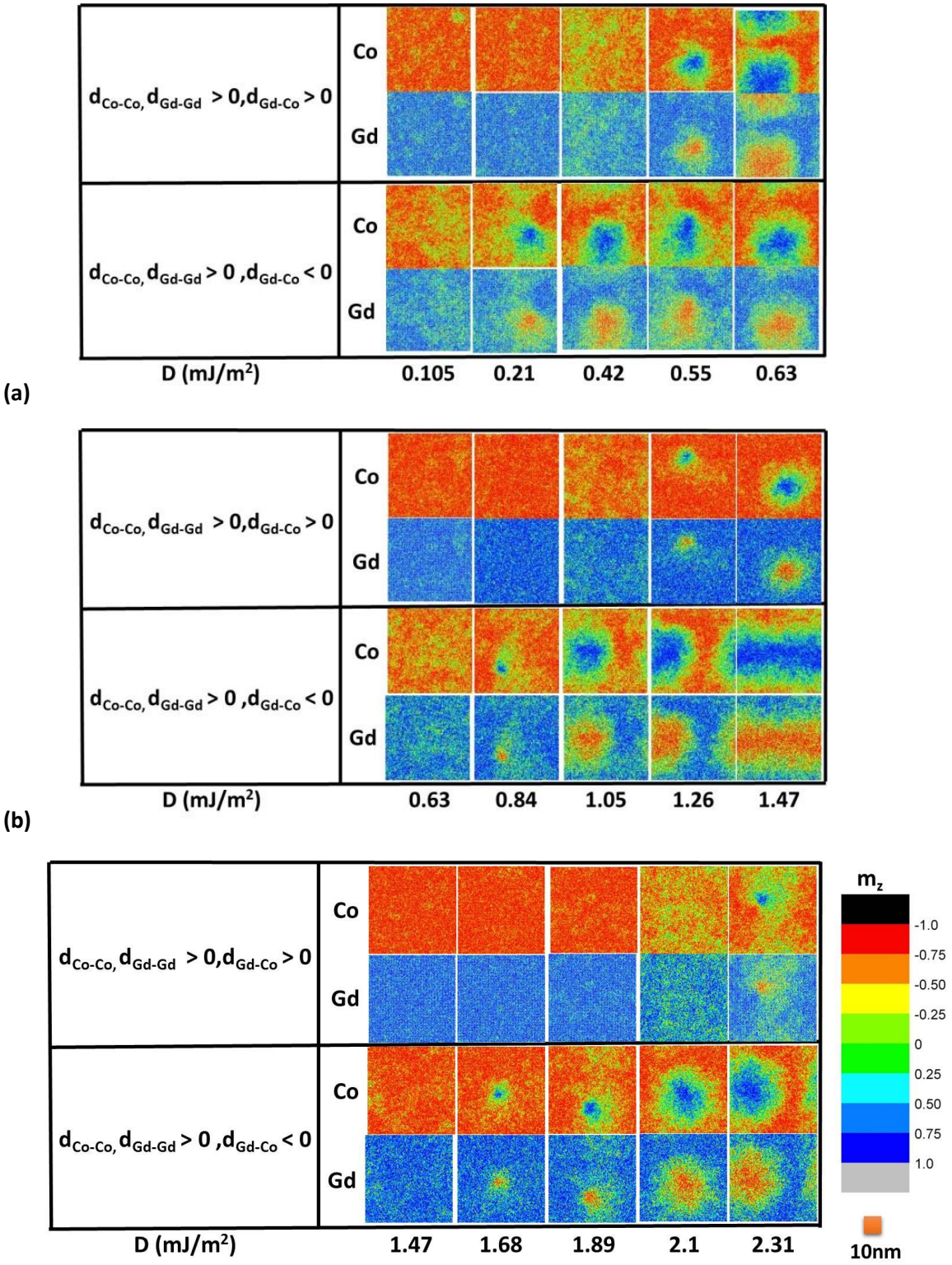

Figure 6.4 Color mapping of equilibrium spin configurations for various DMI values (exponentially decaying DMI) at 300K with T_{comp} = 250 K for $d_{Gd-Co} > 0$ and $d_{Gd-Co} < 0$ in (a) 5 nm, (b) 10 nm, and (c) 15 nm GdCo. Out-of-plane components of reduced

magnetizations (m_z) are mapped in the x-y plane using the color bar shown in (c). Ultra-small skyrmions are revealed in 10 nm and 15 nm GdCo samples.

For 5 nm GdCo, with $d_{Gd\text{-}Co} < 0$, $d_{Co\text{-}Co} < 0.25 \times 10^{-22}$ J, only ferrimagnetic states are observed. At $d_{Co\text{-}Co} > 1.0 \times 10^{-22}$ J, skyrmions are elongated due to the boundary effect in the simulation or stripes states are observed. The range of DMI, where skyrmions are found, is smaller compared to a calculation by Fert *et al.* [96]. This is due to a reduction in anisotropy and exchange stiffness in GdCo. With less DMI energy required to create skyrmions, smaller DMI value is needed to create skyrmions and stripes in FiM. Furthermore, experiment results have measured DMI value greater than 1 mJ/m^2 only at ordered FM/heavy metal interface [89, 90]. The DMI value at amorphous FiM/heavy metal remains unknown. Due to the disorder nature of amorphous materials, the DMI value in amorphous FiM can be much smaller than the DMI value observed in ordered FM.

As shown in Figure 6.4, with ferromagnetic DMI ($d_{Gd\text{-}Gd}$ and $d_{Co\text{-}Co}$) that are positive, two scenarios of AFM DMI ($d_{Gd\text{-}Co}$) are considered. At 300 K, in all thicknesses, larger DMI is needed to form skyrmions with positive $d_{Gd\text{-}Co}$ than with negative $d_{Gd\text{-}Co}$. In 5 nm sample, D = 0.55 mJ/m^2 is needed to stabilize skyrmions with $d_{Gd\text{-}Co} > 0$. In comparison, with $d_{Gd\text{-}Co} < 0$, a smaller DMI of D = 0.21 mJ/m^2 is needed to stabilize skyrmions. Similar behaviors are also found in 10 nm and 15 nm samples. With $d_{Gd\text{-}Co} > 0$, the smallest skyrmions are found at D = 1.26 mJ/m^2 in 10 nm sample and D = 2.31 mJ/m^2 in 15 nm sample. On the other hand, with $d_{Gd\text{-}Co} < 0$, the smallest skyrmions are found at D = 0.84 mJ/m^2 in 10 nm sample and D = 1.68 mJ/m^2 in 15 nm sample.

To understand such intriguing behavior in a FiM, the in-plane spin configurations and the chirality of the skyrmion wall are investigated. Figure 6.5 summarizes the chirality of the skyrmion walls in the Co sublattice. Using $d_{Gd\text{-}Gd}$, $d_{Co\text{-}Co} > 0$, and $d_{Gd\text{-}Co} < 0$, in the Co sublattice, the spins are turning in a counter-clockwise direction across the skyrmion wall. For the Gd sublattice, the spins in the skyrmion wall are also turning counter-clockwise. This can be explained by the DMI in the system. AFM couplings between Gd and Co align the spins of Gd and Co in nearly antiparallel directions, except a small canting due to the presence of DMI. With $d_{Gd\text{-}Gd}$ and $d_{Co\text{-}Co} > 0$, turning counter-clockwise is energetically favorable. However, with $d_{Gd\text{-}Gd}$, $d_{Co\text{-}Co} > 0$, and $d_{Gd\text{-}Co} > 0$, the chirality of the simulated skyrmion wall is found to be the opposite. The DMI torque between the AFM pairs now opposes the DMI torques within each sublattice. In the presence of a stronger inter-sublattice DMI torque, the spins in each sublattice now turn clockwise across the skyrmion wall. To summarize, for $d_{Gd\text{-}Co} < 0$, the skyrmion wall is turning counter-clockwise. The **d** (FM) vector is pointing in the opposite direction of $\mathbf{S_i} \times \mathbf{S_j}$. E_{DMI} (FM) = $\mathbf{d_{ij}} \cdot (\mathbf{S_i} \times \mathbf{S_j})$ is negative, which is favorable. For $d_{Gd\text{-}Co} > 0$, the skyrmion wall is turning clockwise. The **d** (FM) vector and $\mathbf{S_i} \times \mathbf{S_j}$ are pointing in the same direction, resulting in positive E_{DMI} (FM). Identical signs of the DMI energy are also found in the Gd sublattice.

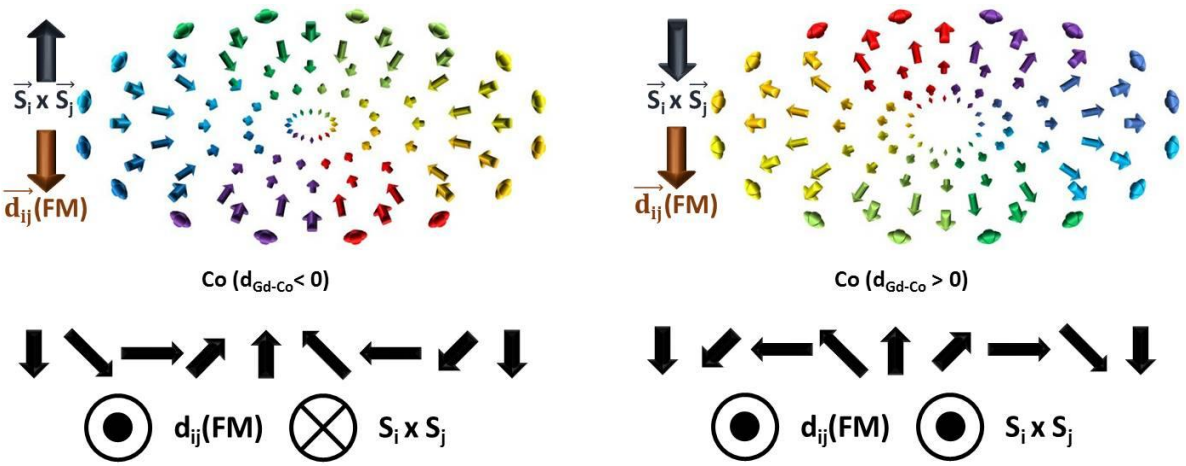

Figure 6.5 Simulated skyrmion configurations of Co sublattice for $d_{Gd\text{-}Co} < 0$ and $d_{Gd\text{-}Co} > 0$ with a metal interface at the bottom. (Top) An overhead view of simulated skyrmion configurations for $d_{Gd\text{-}Co} < 0$ and $d_{Gd\text{-}Co} > 0$. (Bottom)

To better illustrate the change in chirality, the total DMI energies between Co-Co, Gd-Gd, and Gd-Co are computed using the equilibrium configurations at 0 K. Table 6.2 summarizes the sign of the total DMI energies for different nearest neighbor pairs. With $d_{Gd\text{-}Gd}$, $d_{Co\text{-}Co} > 0$ and $d_{Gd\text{-}Co} > 0$, spins are turning counter-clockwise. With this configuration, the total DMI energy between Gd-Gd pair E_{DMI} (Gd-Gd) and Co-Co pair E_{DMI} (Co-Co) are negative, and the total DMI energy between Gd and Co pair E_{DMI} (Gd-Co) is also negative. This means that with $d_{Gd\text{-}Gd}$, $d_{Co\text{-}Co} > 0$, it is energetically favorable for spins to turn counterclockwise. On the other hand, with $d_{Gd\text{-}Gd}$, $d_{Co\text{-}Co} > 0$, and $d_{Gd\text{-}Co} > 0$, spins are revealed to turn clockwise from the simulated configurations. As a result of the sign change in chirality, E_{DMI} (Gd-Gd) and E_{DMI} (Co-Co) become positive. On the other hand, E_{DMI} (Gd-Co) remains negative because both chirality and $d_{Gd\text{-}Co}$ changes sign. This implies that it is energetically favorable for Gd-Co pair to turn clockwise across, but it is energetically unfavorable for Gd-Gd and Co-Co pairs to do so. In other words, AFM DMI $d_{Gd\text{-}Co}$ is able to overcome ferromagnetic DMI $d_{Gd\text{-}Gd}$ and $d_{Co\text{-}Co,}$ resulting in energy favorable configurations for Gd-Co pairs. To summarize, in a FiM, if the DMI of

ferromagnetic pair and AFM pair have the same sign, a cancellation of DMI occurs because it is preferable for a ferromagnetic pair to turn in the opposite direction of an AFM pair. No cancellation occurs if the DMI of ferromagnetic pair and AFM pair have the opposite sign. These also explain the differences in the size of skyrmion between $d_{Gd\text{-}Co} < 0$ and $d_{Gd\text{-}Co} > 0$. The $d_{Gd\text{-}Co} < 0$ scenario has larger skyrmions because both ferromagnetic and AFM pairs are contributing to the formation of a skyrmion, which means the DMI effect is stronger overall.

Scenario	E_{DMI}(Gd-Gd)	E_{DMI}(Co-Co)	E_{DMI}(Gd-Co)
$d_{Gd\text{-}Gd}$, $d_{Co\text{-}Co} > 0$, $d_{Gd\text{-}Co} < 0$	-	-	-
$d_{Gd\text{-}Gd}$, $d_{Co\text{-}Co} > 0$, $d_{Gd\text{-}Co} > 0$	+	+	-

Table 6.2 Sign of total DMI energy E_{DMI} computed from equilibrium spin configurations at 0 K.

6.3.1 Skyrmion Phase Diagram in GdCo

To investigate the minimal size of room temperature skyrmions in GdCo, D-K phase diagrams with exponentially decaying DMI at 300 K are simulated for 5, 10, and 15 nm GdCo films. In this section, we focus on the $d_{Gd\text{-}Co} < 0$ scenario. Since the energy barrier is a function of exchange stiffness and thickness [97], the minimal skyrmions size found in $d_{Gd\text{-}Co} < 0$ scenario can also apply to $d_{Gd\text{-}Co} > 0$ scenario, except a larger DMI is required. For each thickness, anisotropy ranges from 0.05×10^5 J/m^3 to 4×10^5 J/m^3 are investigated. Experimentally, GdCo has anisotropy in the order of 10^4 J/m [5,6,16] For DMI, larger interfacial DMI is explored in thicker samples, because as thickness increases, the average DMI decreases, and larger interfacial DMI is needed to stabilize skyrmions. In 5 nm samples, interfacial DMI of 0 to 2 mJ/m^2, which corresponds to $d_{Co\text{-}Co}$ of 0 to 2.38×10^{22} J, are investigated. Figure 6.6 (a) shows the D-K phase diagram of 5 nm GdCo at 300 K. In 5 nm GdCo, skyrmions, range from 12 nm to 40 nm, are stabilized

in the simulated range of interfacial DMI and anisotropy. Lines of 15 to 30 nm indicate the size of skyrmions at various DMI and anisotropy. As DMI decreases or anisotropy increases, skyrmions become smaller and eventually collapse into FiM states. At the opposite side of D-K diagram, with large DMI and small anisotropy, skyrmions larger than 40 nm become elongated or collapsed due to the boundary of the simulation space (50.7 nm x 50.7 nm). This elongation of skyrmions was also seen earlier in Figure 6.4 at large DMI values. Overall, for a given anisotropy, as interfacial DMI increases from 0 to 2.0 mJ/m^2, the equilibrium configuration goes from FiM to skyrmions, then to stripes. For a fixed DMI, as anisotropy increases, the size of skyrmions decreases, and finally, skyrmions collapse into FiM states. These behaviors of skyrmions in FiM GdCo as a function of DMI and anisotropy is the same as what has been observed in a ferromagnet [97, 98].

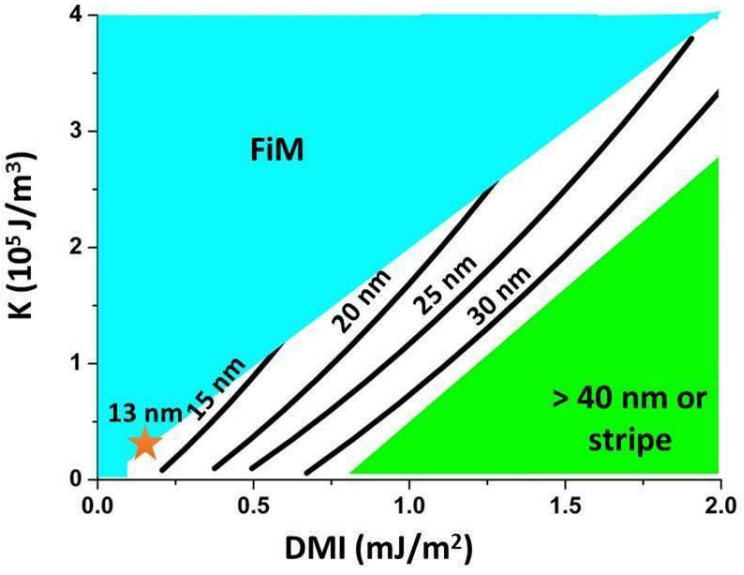

(a)

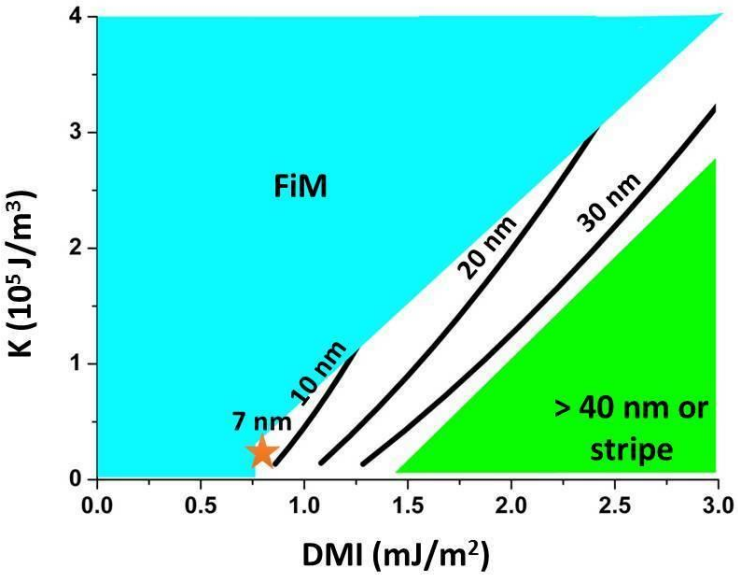

(b)

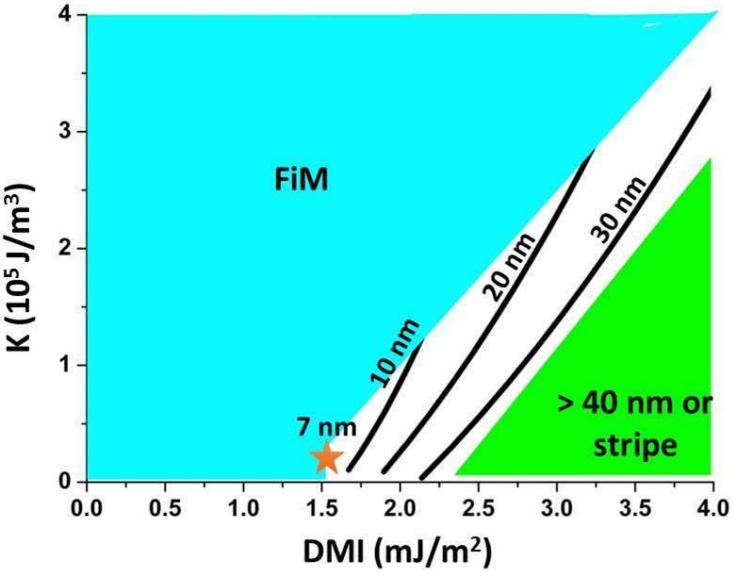

(c)

Figure 6.6 D-K phase diagram of (a) 5 nm, (b) 10 nm and (c) 15 nm GdCo at 300 K with $d_{Gd\text{-}Co} < 0$ and T_{comp} = 250 K. Star corresponds to smallest skyrmions simulated at K = 0.3 x 10^5 J/m^3.

For 10 nm and 15 nm GdCo, DMI of 0 to 3 mJ/m^2 (d_{Co-Co} of 0 to 3.57 x 10^{22} J) and 0 to 4 mJ/m^2 (d_{Co-Co} of 0 to 4.76 x 10^{22} J) are explored respectively. The overall trend of skyrmions as a function of DMI and anisotropy in 10 nm and 15 nm GdCo are identical to that of the 5 nm GdCo, where an increase in DMI leads to larger skyrmions, and increase in anisotropy results in smaller skyrmions. However, one important difference is observed in thicker samples, where ultra-small skyrmions as small as 7 nm are stable at room temperature. For both 10 nm and 15 nm GdCo, there is a region of DMI and anisotropy where ultra-small skyrmions are stabilized. In 10 nm GdCo, ultra-small skyrmions are found in the region of DMI ranges from 0.8 to 1.0 mJ/m^2, and anisotropy ranges from (0.1 to 0.8) x 10^5 J/m^3. For 15 nm GdCo, this region lays within DMI ranges from 1.5 to 1.8 mJ/m^2, and anisotropy ranges from (0.1 to 1.0) x 10^5 J/m^3. For both 10 nm and 15 nm GdCo, the anisotropy falls within the same range as what has being measured experimentally in GdCo [5, 6, 16], which is in the order of 10^4 J/m^3. However, the interfacial DMI is much less than what has been observed at a Pt interface. Interfacial DMI of up to 12 mJ/m^2 is reported at a Pt/Co interface [99]. Thus, some reductions of DMI from that of Pt are needed to obtain ultra-small skyrmion in GdCo films in experiments. The reduction of DMI can be obtained by sandwiching GdCo between two Pt layers with one Pt layer being diluted by other elements. Since GdCo is amorphous, we have more flexibility in tuning the underlayer and the capping layer of a multilayer sandwich. With its intrinsic anisotropy and flexibility, GdCo films are promising materials to obtain ultra-small skyrmions at room temperature through DMI tuning.

Further tuning of skyrmions can be obtained through varying thicknesses and T_{comp}. Figure 6.7 shows the thickness-T_{comp} phase diagram for anisotropy K = 0.3 x 10^5 J/m^3 and

interfacial DMI $D_0 = 0.9$ mJ/m^2. As mentioned before, K = 0.3 x 10^5 J/m^3 is the measured anisotropy in GdCo. In Figure 6.7, the thickness is varied from 5 nm to 10 nm. As thickness increases from 5 nm to 10 nm, skyrmions size decreases, and some dissolved into the ferrimagnetic state. This behavior can be explained by the effectiveness of the interfacial DMI. As thickness increases, for a fixed interfacial DMI, the average DMI decreases, and the overall effectiveness of interfacial DMI is reduced. With smaller DMI, skyrmions are expected to decrease and eventually disappear.

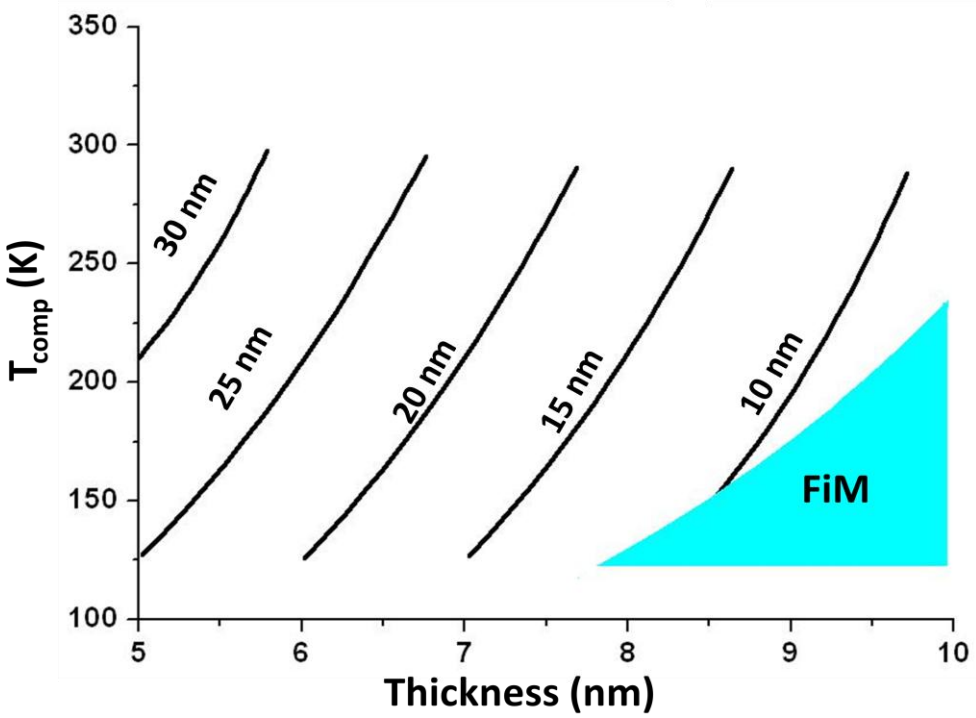

Figure 6.7 Thickness-T_{comp} phase diagram at 300 K with K = 0.3 x 10^5 J/m^3 and $D_0 = 0.9$ mJ/m^2 with $d_{Gd\text{-}Co} < 0$.

Another worth-noting property reveals in the thickness-T_{comp} is the existence of sub-10 nm skyrmion at room temperature. As discussed earlier, an increase in thickness increases the stability of skyrmions, and smaller skyrmions are stable at room temperature. Alone the T_{comp} axis, T_{comp} is varied from 125 K to 300 K. For a given

thickness, as T_{comp} increases, the size of skyrmions increase. For example, at 5 nm, skyrmion size goes from 25 nm to 35 nm, as T_{comp} increases from 125 K to 300 K. This behavior can be explained by both the exchange interaction and demagnetization energy, with the main contribution comes from exchange interaction. To increase the T_{comp}, the concentration of Co must be decreased. Since Co has a higher Curie temperature than Gd, exchange interactions are stronger in the Co sublattice. With a weaker overall exchange interaction, skyrmions are expected to become larger. Furthermore, as T_{comp} moves away from 300 K, the magnetization of GdCo increases and the demagnetization energy begins to have an influence in skyrmion formation, which can reduce the skyrmion size.

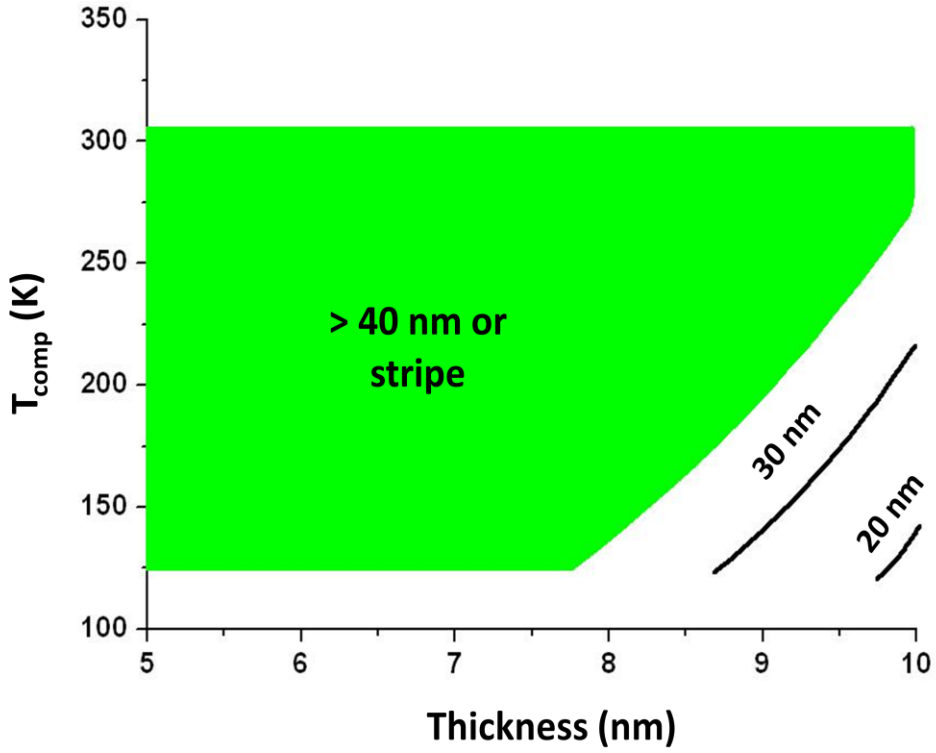

Figure 6.8 Thickness-T_{comp} phase diagram at 300 K with K = 0.3 x 10^5 J/m^3 and D_0 = 1.5 mJ/m^2 with $d_{Gd\text{-}Co} < 0$.

Figure 6.8 shows the thickness- T_{comp} phase diagram at 300 K with K = 0.3 x 10^5 J/m^3 and D_0 = 1.5 mJ/m^2, a larger DMI compared to Figure 6.7. In this phase diagram, with D_0 = 1.5 mJ/m^2, the interfacial DMI appears to be too large for small skyrmion formation. However, one can increase the thickness to reduce the average DMI to form smaller skyrmions at room temperature. Skyrmion of below 20 nm can stabilize at 10 nm thickness. Further increases in thickness to 15 nm, as shown in Figure 6.6 (c), can reduce the skyrmions to 7 nm. This tuning of thickness and DMI leads us to the next set up phase diagram, in thickness-DMI space.

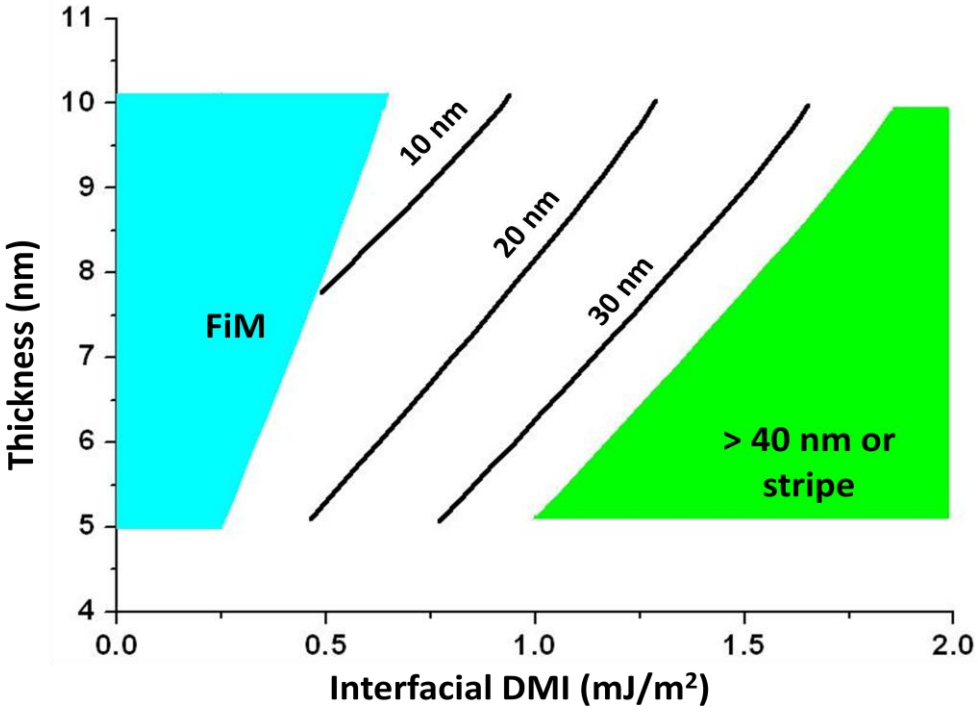

Figure 6.9 DMI-Thickness phase diagram at 300 K with K = 0.3 x 10^5 J/m^3 and T_{comp} = 250 K with $d_{Gd\text{-}Co} < 0$.

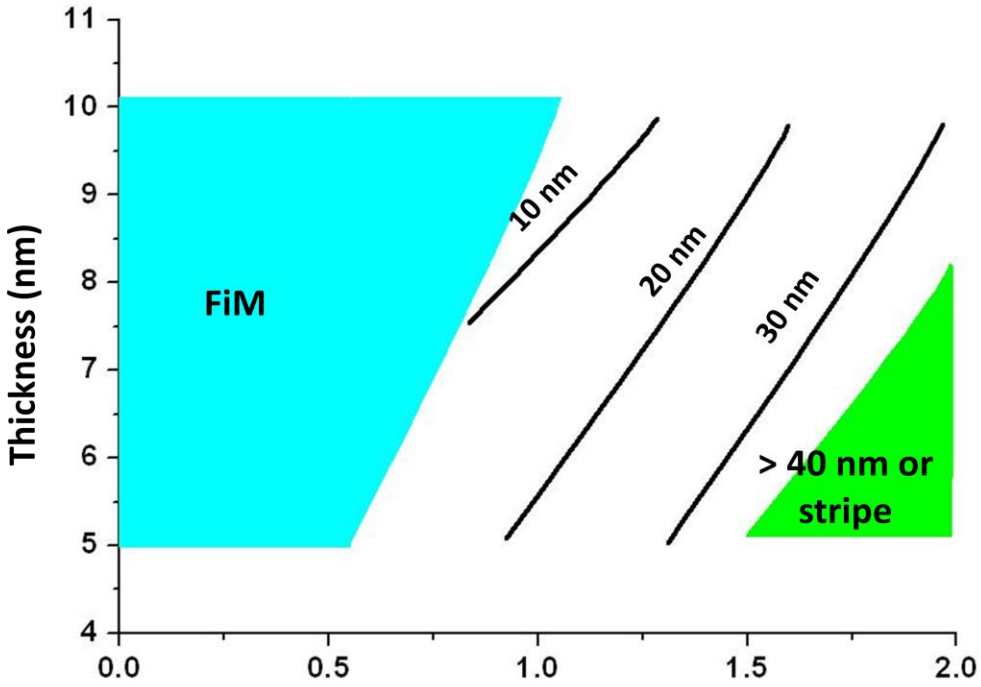

Figure 6.10 DMI-Thickness phase diagram at 300 K with K = 0.3 x 10^5 J/m^3 and T_{comp} = 130 K with $d_{Gd\text{-}Co} < 0$.

In Figure 6.9, the DMI-Thickness phase diagram at 300 K with K = 0.3 x 10^5 J/m^3 and T_{comp} = 250 K is plotted. Figure 6.9 shows that for a given DMI, an increase in thickness can reduce the skyrmions and increase the stability of ultra-small skyrmions. Sub 10 nm skyrmions are found in the thickness of 8 to 10 nm and interfacial DMI of 0.5 to 0.7 mJ/m^2. In Figure 6.10, the DMI-Thickness phase diagram at 300 K with K = 0.3 x 10^5 J/m^3 is plotted, where T_{comp} is reduced to 130 K. In this sample, sub 10 nm skyrmions are found in the thickness of 8 to 10 nm and interfacial DMI of 0.9 to 1.1 mJ/m^2. Overall, a threshold of at least 8 nm is needed to host sub 10 nm skyrmions.

To summarize, various parameters, includes thickness, T_{comp}, anisotropy, and DMI, are tuned to determine the optimal parameters space for ultra-small skyrmions at room temperature. For GdCo, favorable conditions are the thickness of at least 8 nm and

interfacial DMI of 0.5 mJ/m^2 or more. Depends on the DMI, either higher or lower T_{comp} can be beneficial. For larger DMI of 1.0 mJ/m^2, a lower T_{comp} to 130 K is more favorable and vice versa. In an experiment, thickness and T_{comp} are easier parameters to control. Thickness can be easily controlled through deposition time, and T_{comp} can be tuned through composition. For DMI, it may be reduced using dilution in the heavy metal interface. For anisotropy, it is pretty much fixed for the given RE-TM films, and tuning will require doping of another element in the thin films.

6.3.2 Tomograph of a Skyrmion in GdCo

For device applications, especially in thicker films, we will also need to consider the growth of skyrmions away from the interface. With decaying DMI away from the interface, spins at the top of a thicker sample experience effectively zero DMI. Without DMI, one might expect spins near the top to align parallel for FM neighbors and antiparallel for AFM neighbors, and skyrmions to disappear far away from the interface. If skyrmions collapse far away from the interface, the reliability of such memory devices would be vastly reduced. To investigate whether skyrmions remain robust in thicker samples, a numerical tomography is employed to image simulated ultra-small skyrmions at 300 K. Figure 6.7 shows the numerical tomography plot of an ultra-small skyrmion in 10 nm GdCo. This skyrmion corresponds to D = 0.84 mJ/m^2 and K = 0.3 x 10^5 J/m^3. The same skyrmion was shown in Figure 6.4 (b) and as the smallest skyrmions (Star Symbol) at K = 0.3 x 10^5 J/m^3 in Figure 6.6 (b) In the 3D plots at the center of Figure 6.11, colors are made to be somewhat transparent to reveal the skyrmions structure near the center. For the Co sublattice, red to orange color shows that most of the spins are pointing down. A region of green and blue that appears near the center corresponds to the simulated

skyrmion at 300 K. As evidenced by the columnar distribution of blue color, the skyrmion retains a uniform columnar growth from the bottom to the top. Columnar distribution of skyrmion is also found in the Gd sublattice, where a column of red is distributed uniformly from the bottom to the top.

To further demonstrate the uniform columnar distribution of skyrmion, in-plane and out-of-plane cross-sections of the skyrmion are also plotted in Figure 6.11 On the left of Figure 6.11, the in-plane cross-section of spin configuration within 0.5 nm of the interface and 0.5 nm of the top are mapped. The skyrmions at the interface and near the top have identical sizes and shapes. Compare to the mapping of spin configurations in Figure 6.4 (b), the size of the skyrmion remains the same. This shows that the size of skyrmions remains uniform throughout a sample. On the right side of Figure 6.11, the out-of-plane cross-sections are shown for the Gd and Co sublattices. The blue color in the Co sublattice and the red color in the Gd sublattice correspond to the center of the skyrmion. For both sublattices, the out-of-plane cross-sections show a columnar distribution of skyrmion from the bottom interface to the top. These results provide important pieces of evidence that skyrmion remains robust through a thicker sample and further support of using thicker GdCo samples to increase skyrmion stability at room temperature.

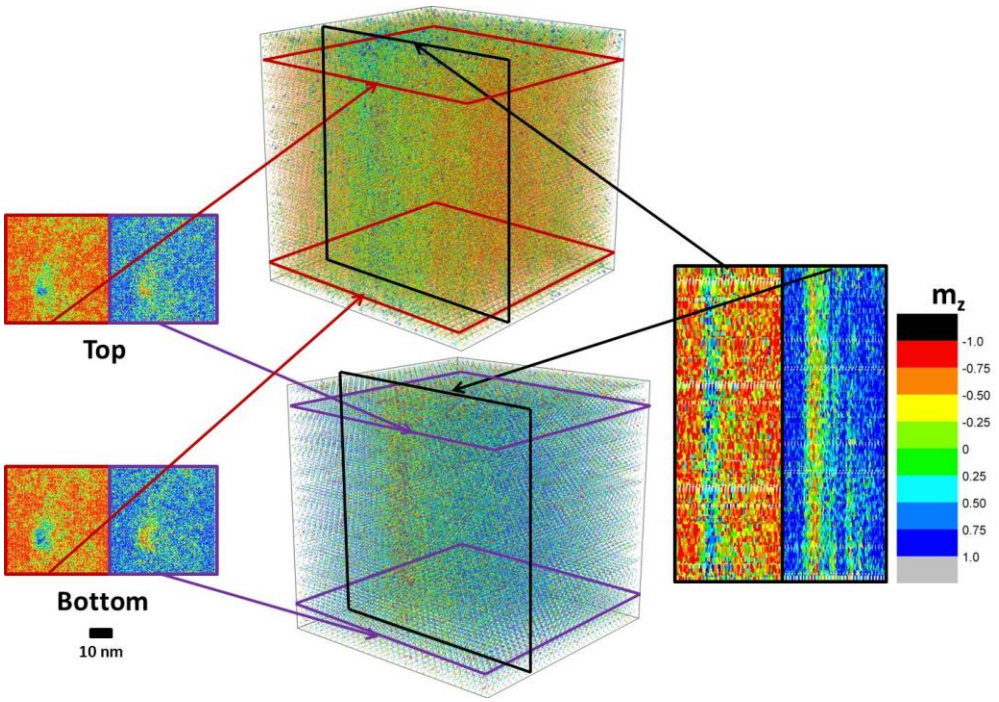

Figure 6.11 Tomograph of a simulated ultra-small skyrmion in 10 nm GdCo at 300 K. It reveals columnar skyrmion distribution throughout the 10 nm GdCo sample. The figure shows Co-sublattice spins (top box), Gd-sublattice spins (bottom box), in-plane cross-sections of near the top and bottom interface (left), and out-of-plane cross-sections (right).

6.4 Mixing Layer in Amorphous Ferrimagnets (Collaboration with NIST)

In collaboration with Dr. Brian Kirby at NIST, we have employed polarized neutron reflectometry (PNR) [100,101] to investigate the interfacial properties of a W/Pt/GdCo (5 nm)/W/Pt heterostructure deposited on a Si /SiO2 substrate. Figure 6.12 shows temperature-dependent depth profiles determined from measurements taken in an in-plane 3 T field. The top panel shows the profiles in terms of scattering length density, while the bottom panel shows the in-plane magnetization profiles. The GdCo layer exhibits an inhomogeneous magnetization profile at all temperatures. Near the Pt/GdCo

interface, a 2 nm region shows a different temperature-dependent magnetization from the rest of the sample.

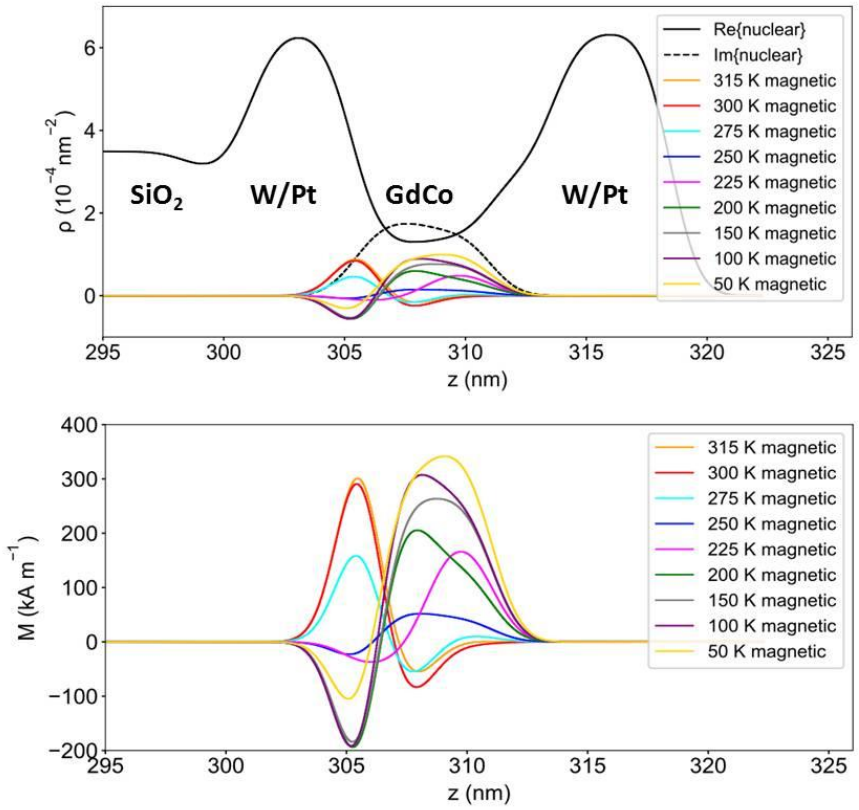

Figure 6.12 Scattering length density (top) and magnetization vs. temperature (bottom) of W/Pt/GdCo (5 nm)/W/Pt on SiO_2 substrate.

Figure 6.13 summarizes the magnetization as a function temperature for the mixing layer and the "bulk" layer (rest of the sample). T_{comp} of the entire of GdCo is found to be near 260 K. Both the mixing layer and the rest of the sample appear to show vanishing magnetization corresponds to T_{comp} near 260 K. The difference in temperature-dependent magnetization likely arises from the intermixing of Pt and GdCo at the interface. With this mixing layer, the robustness of skyrmion in these heterostructures may be compromised. To address this issue, this mixing layer is incorporated into the simulation in section 6.4.

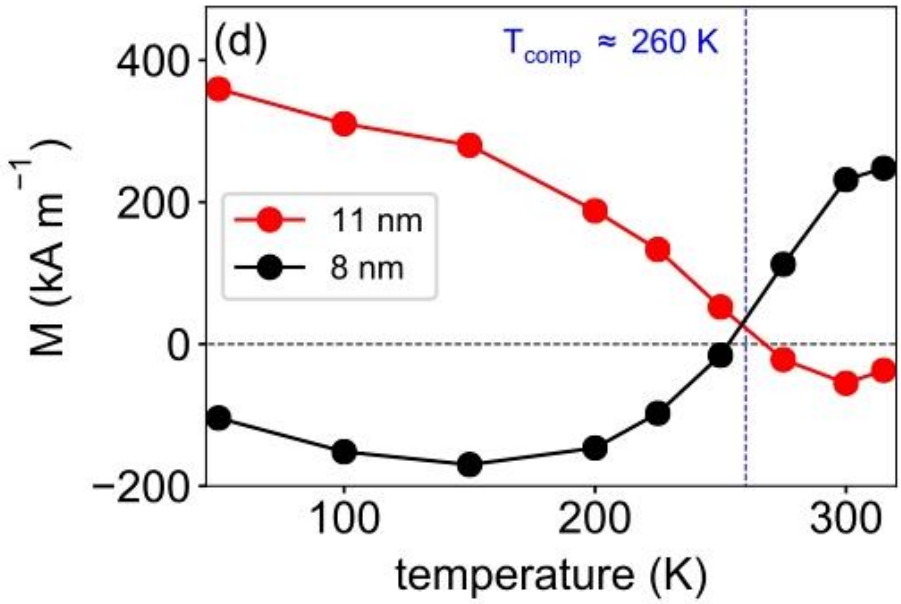

Figure 6.13 Summary of magnetization as a function for the mixing layer (black line) and the rest of the sample (red line).

6.5 Effect of Mixing Layer in Skyrmions Formations

From Figure 6.13, the mixing layer appears to cross compensation near 260 K, where magnetization vanishes. Upon further inspection, the magnetization is negative below T_{comp}, which means it is still dominated by the Co sublattice. In comparison, the rest of the sample shows positive magnetization above T_{comp}, which means it is dominated by the Gd sublattice. Below 100 K, the absolute value of magnetization |M| in the mixing layer begins to decrease. This suggests either the Co sublattice is weakening or the Gd sublattice is strengthening. Since the Co sublattice has a high Curie temperature, it must be the strengthening of the Gd sublattice that causes a decrease in |M|. A hypothesis is that the T_{comp} near 260 K is an artifact due to the vanishing magnetization of the entire sample, which has T_{comp} near 260 K. In PBR measurement, an in-plane field of 3 T is utilized to saturate the samples. Across $T_{comp,}$ spins are flipped. Since the magnetization is

near 0 around $T_{comp,}$ 3 T in-plane field fails to saturate the spins. As a result, domains are formed in the bulk layer. With exchange interaction, the mixing layer also breaks into domains and leads to vanishing magnetization. To test this idea, the micromagnetic model OOMMF is employed [27]. Table 6.3 listed the parameter used in the simulation.

Parameter	Value
Cell Size	2 nm x 2 nm x 1 nm
Size of Mixing Layer	500 nm x 500 nm x 2 nm (250 x 250 x 2)
M_s of Mixing Layer	180 emu/cc
Size of Bulk Layer	500 nm x 500 nm x 3 nm (250 x 250 x 3)
M_s of Mixing Layer	5 emu/cc
K_u of Both Layer	3×10^{4} J/m^{3}
Exchange stiffness (Both)	1.5×10^{11} A/m
Magnetic Field	In-plane 3 T (+y)

Table 6.3 Values of parameters used in the OOMMF to test vanishing magnetization in the mixing layer at T_{comp}

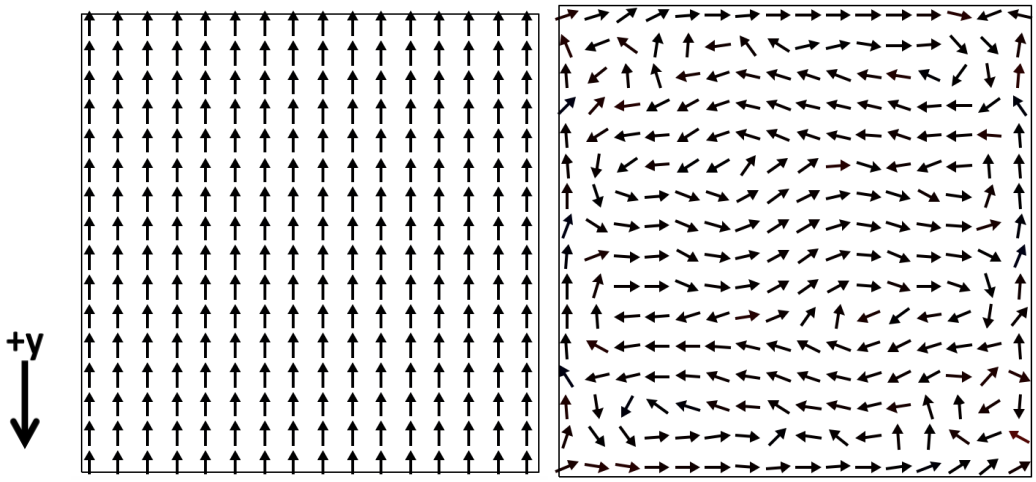

Figure 6.14 Initial (left) and final (right) spin configuration of the mixing layer.

To follow PNR experiments, we begin with magnetization aligns in -y direction and then turns on a 3 T magnetic field to flip the spins across the compensation. Without the bulk layer, a 3 T in-plane field is large enough to saturate the spins in the mixing layer. With the bulk layer, a 3 T in-plane field is not enough to saturate the spins, resulting in a

spiral/domain in both layers. This will lead to an apparent T_{comp} in the mixing layer near 260 K. This means that if the mixing layer separately, the T_{comp} will be below 50 K and not 260 K.

Based on results from PNR and OOMMF simulations, we build a heterostructure model in atomistic simulation to investigate the effect of such a mixing layer on skyrmion. We employ a heterostructure of two T_{comp} to investigate the effect of the mixing layer on skyrmions in GdCo. Figure 6.16 shows the simulated heterostructure. In this model, the mixing layer is assumed to be mixed with Pt, and a decrease in Gd concentration. The composition of the mixing layer is $(Gd_{23}Co_{77})_{75}Pt_{25}$. The reason behind this model is that during the beginning of the sputtering deposition, the adhesion of Co atoms on Pt could be more favorable in comparison to Gd atoms. This is because Gd is large atoms, and it is harder to stick on to Pt atoms. Furthermore, T_{comp} also decreases to below 50 K, which agrees with PNR and OOMMF modeling.

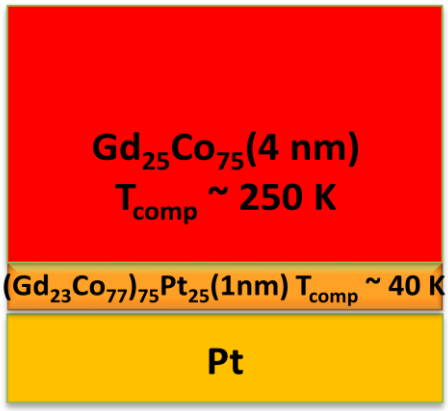

Figure 6.16 Simulated heterostructure of GdCo with 1 nm mixing.

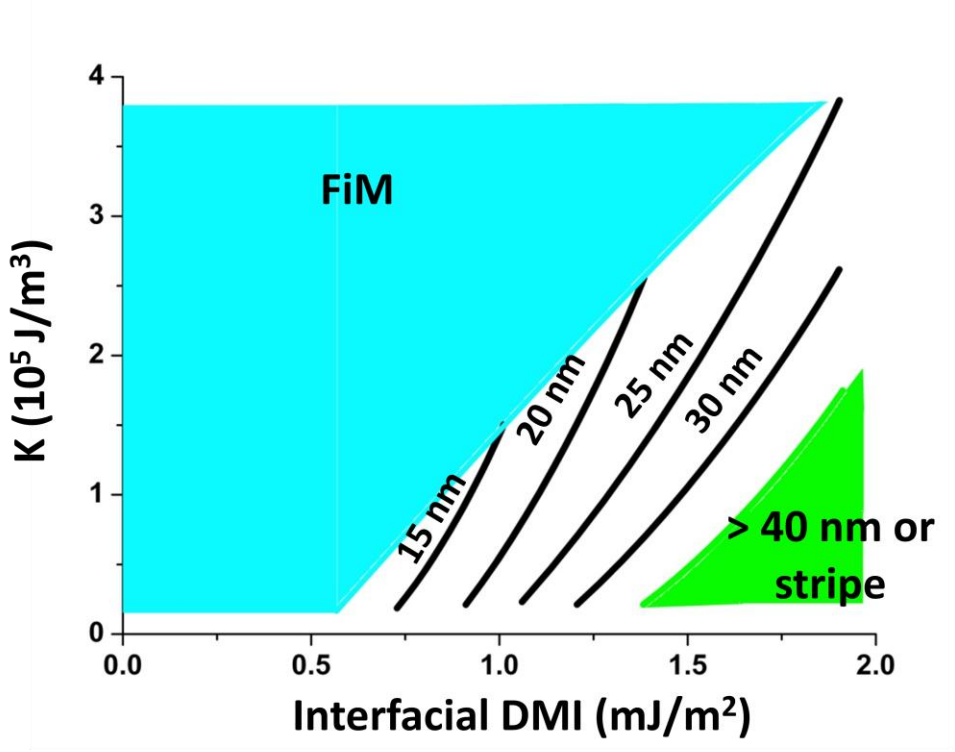

Figure 6.17 DMI-anisotropy phase diagram at 300 K of W/Pt/GdCo(5 nm)/W/Pt on SiO_2 substrate with mixing layer. The heterostructure used in the simulation is shown in Figure 6.16

Figure 6.17 shows the DMI-anisotropy phase diagram of 5 nm GdCo with 1 nm$(Gd_{23}Co_{77})_{75}Pt_{25}$ mixing layer. The skyrmions size has a similar behavior to the 5 nm GdCo without the mixing layer, as shown in Figure 6.6 (a). With or without mixing layer, small skyrmions close to 13 nm are stable at room tempearture. This means the mixing layer has little to no effect on skyrmion stability. However, with the mixing layer, a larger DMI of 0.75 mJ/m^2 is needed to obtain 15 nm skyrmion, comparing to 0.25 mJ/m^2. Although a larger DMI is needed to stabilize skyrmions, it might turn out to be beneficial. As discussed earlier, the measured interfacial DMI in Pt/Co is close to 1 mJ./m^2 [88, 89]. With such DMI, simulations find a skyrmion size of about 22 nm with K = 0.3 x 10^5 J/m^3 in 5 nm GdCo with the mixing layer. Without the mixing layer, large skyrmions of more

than 40 nm are found in the simulations. Therefore, it is more likely to obtain small skyrmions in GdCo with the mixing layer. In section 6.3, simulation proposes the use of a thicker sample over 8 nm. Since the mixing layer only presents at the interface, the effect of the mixing layer decreases as thickness increases. Thus, even with mixing, the using of a thicker sample over 8 nm is still crucial for ultrasmall skyrmions

To further demonstrate the robustness of skyrmions in GdCo with mixing, we further increase the thickness of the mixing layer to 2 nm and employ numerical tomograph to investigate the structure of skyrmions. Figure 6.18 shows the numerical tomograph of 5 nm GdCo with a 2 nm mixing layer. In both Gd and Co sublattice, a columnar distribution of a skyrmion has revealed. This proves that even with the 2 nm mixing layer, skyrmions remain robust throughout 5 nm GdCo.

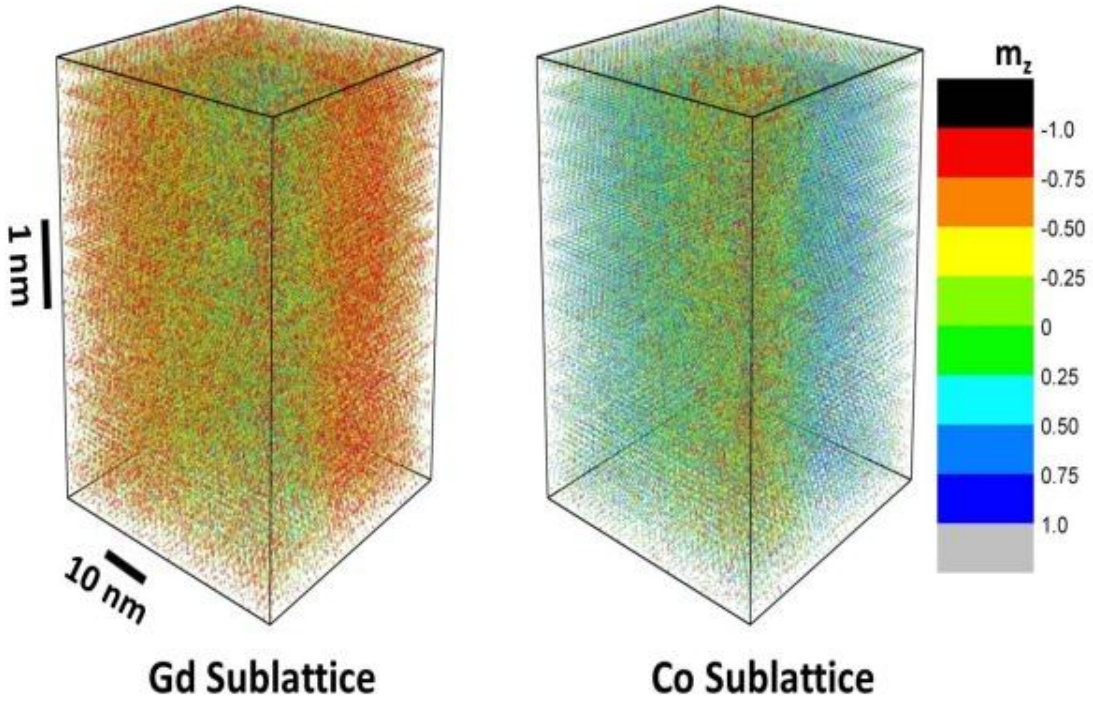

Figure 6.18 Numerical tomograph of a skyrmion in 5 nm GdCo with a 2 nm mixing layer of $(GdCo)_{75}Pt_{25}$. Color is mapped based on out-of-plane reduced magnetization (m_z) of each spin

6.6 Summary

Using atomistic stochastic LLG simulations, ultra-small skyrmions are shown to be stable at room temperature in ferrimagnetic GdCo. Despite the rapid decay of Dzyaloshinskii Moriya interaction (DMI) away from the interface, a realistic range of DMI values is seen to stabilize skyrmions in GdCo films as thick as 15 nm irrespective of the sign of DMI between antiferromagnetic coupled Gd and Co, Furthermore, the low DMI values needed to form ultra-small skyrmion in GdCo indicate opportunity for designing magnetic materials to host ultra-small Neel skyrmions. Through tomography of an ultra-small skyrmion in 10-nm thick GdCo film, it is discovered that the skyrmion assumes a columnar configuration that extends uniformly across the film thickness despite having near-zero DMI far away from the interface. Furthermore, collaboration with Dr. Brian J. Kirby at NIST reveals the presence of a mixing layer at the Pt/GdCo interface. Despite the mixing layer, skyrmions are found to be robust and may even be beneficial for the forming of ultra-small skyrmions. These findings argue for using thicker magnetic films to host ultra-small skyrmions, providing an important strategy for developing high density and high-efficiency skyrmion based devices.

7. Summary and Future Work

In summary, this thesis is a computation and experimental study of amorphous RE-TM thin films. Modeling techniques discussed in Chapter 3 of the thesis successfully verified experimental results and provided guidance on future experiments.

In Chapter 4, using the two-sublattice model, the exchange bias effect in TbFeCo has been proven to originate from the exchange anisotropy between the two nanoscale amorphous phases. This model can be employed to study the exchange bias effect in other intrinsic two-phase systems, such as Mn-Pt-Ga. Furthermore, the sub-lattice model is not limited to study the exchange bias effect. It can be applied to any ferrimagnetic systems to reduce the computational time compared to atomistic simulations.

The tuning of magnetic anisotropy through interfacial has been shown in Chapter 5. The results from VO_2/TbFeCo provide a pathway to tune and develop devices using MIT of VO_2.

Finally, Chapter 6 presented a computational study on skyrmions in GdCo at room temperature. Atomistic simulations found that an increase in GdCo thickness to at least 8 nm is necessary to obtain sub 10 nm skyrmions. Experimental works are currently underway on thicker GdCo films to verify these findings. For the atomistic model, future works include studying the spin dynamics of skyrmions with the mixing layer. One might think that having such a mixing layer causes significant disruption in moving skyrmions in devices. With the atomistic model, this intuition can be tested to determine if there are any unexpected results. Furthermore, tuning of magnetic properties can be achieved by

elemental doping. Using the atomistic model, one can explore the different possibilities of doping or even a completely different system for skyrmion based devices.

References

[1] C. D. Stanciu, A. V. Kimel, F. Hansteen, A. Tsukamoto, A. Itoh, A. Kirilyuk, and Th. Rasing. Ultrafast spin dynamics across compensation points in ferrimagnetic GdFeCo: The role of angular momentum compensation. *Phys. Rev. B* **73**, 220402(R) (2006).

[2] I. Radu, K. Vahaplar, C. Stamm, T. Kachel, N. Pontius, H. A. Dürr, T. A. Ostler, J. Barker, R. F. L. Evans, R. W. Chantrell, A. Tsukamoto, A. Itoh, A. Kirilyuk, Th. Rasin, and A. V. Kimel. Transient ferromagnetic-like state mediating ultrafast reversal of antiferromagnetically coupled spins. *Nature* **472**, 205-208 (2011).

[3] A. Hassdenteufel, B. Hebler, C. Schubert, A. Liebig, M. Teich, M. Helm, M. Aeschlimann, M. Albrecht, and R. Bratschitsch. Thermally Assisted All-Optical Helicity Dependent Magnetic Switching in Amorphous $Fe_{100-x}Tb_x$ Alloy Films *Adv. Mater*. **25** 3122-3128 (2013).

[4] M. Nakayama, T. Kai, N. Shimomura, M. Amano, E, Kitagawa, T. Nagase, M. Yoshikawa, T. Kishi, S. Ikegawa, and H. Yoda. Spin transfer switching in TbCoFe/CoFeB/MgO/CoFeB/TbCoFe magnetic tunnel junctions with perpendicular magnetic anisotropy. *J. Appl. Phys*. **103**, 07A710 (2008).

[5] F. Tanaka, S. Tanaka, and N. Imamura. Magneto-optical recording characteristics of TbFeCo media by magnetic field modulation method. *Jpn. J. Appl. Phys*. **26**, 231 (1987).

[6] P. Hansen, C. Clausen, G. Much, M. Rosenkranz, and K. Witter. P. Hansen, C. Clausen, G. Much, M. Rosenkranz, and K. Witter, *J. Appl. Phys*. **66**, 756 (1989).

[7] S. Tsunashima, Magneto-optical recording. *J. Phys. D. Appl. Phys*. **34**, R87 (2001).

[8] S.H. Charap, P-L Lu, and Y. He. Thermal stability of recorded information at high densities. *IEEE Trans. Magn.* **33,** 978–983 (1997).

[9] N. Nishimura, T. Hirai, A. Koganei, T. Ikeda, K.Okano, Y. Sekiguchi, and Y. Osada. Magnetic tunnel junction device with perpendicular magnetization films for high-density magnetic random access memory. *J. Appl. Phys.* **91,** 5246–5249 (2002).

[10] M. Ding and S. J. Poon. Tunable perpendicular magnetic anisotropy in GdFeCo amorphous films. *J. Magn. Magn. Mater.* **339**, 51-55 (2013).

[11] C. Schubert, A. Hassdenteufel, P. Matthes, J. Schmidt, M. Helm, R. Bratschitsch and M. Albrecht. All-optical helicity dependent magnetic switching in an artificial zero moment magnet. *Appl. Phys. Lett.* **104**, 082406 (2014).

[12] S. Mangin, M. Gottwald, C-H. Lambert, D. Steil , V. Uhlíř , L. Pang , M. Hehn, S. Alebrand, M. Cinchetti, G. Malinowski, Y. Fainman, M. Aeschlimann, and E. E. Fullerton. Engineered materials for all-optical helicity-dependent magnetic switching. *Nat. Mater.* **13**, 286 (2014).

[13] B. Hebler, A. Hassdenteufel, P. Reinhardt, H. Karl, and M. Albrecht. Ferrimagnetic Tb–Fe Alloy Thin Films: Composition and Thickness Dependence of Magnetic Properties and All-Optical Switching. *Front. Mater.* **3,** 8 (2016).

[14] A. Kirilyuk, A. V. Kimel, and T. Rasing, Ultrafast optical manipulation of magnetic order. *Rev. Mod. Phys*. **82**, 2731–2784 (2010).

[15] A. Kirilyuk, A. V. Kimel, and T. Rasing. Laser-induced magnetization dynamics and reversal in ferrimagnetic alloys *Rep. Prog. Phys*. **76**, 026501 (2013).

[16] L. Caretta, M. Mann, F. Büttner, K. Ueda, B. Pfau, C. M. Günther, P. Hessing, A. Churikova, C. Klose, M. Schneider, D. Engel, C. Marcus, D. Bono, K. Bagschik, S. Eisebitt, and G. S. D. Beach. Fast current-driven domain walls and small skyrmions in a compensated ferrimagnet. *Nat. Nanotechnol.* **13**, 1154-1160 (2018).

[17] L.J. Van der Pauw. A method of measuring the resistivity and Hall coefficient on lamellae of arbitrary shape. *Philips Technical Review* **20**: 220–224 (1958).

[18] P, Sigmund. in Sputtering by Ion Bombardment Vol. 1 (ed. E. Berisch) 9-71 (Springer, New York, 1981).

[19] P.J. Kelly, and R.D Arnell. Magnetron sputtering: a review of recent developments and applications.*Vacuum* **56** 159-172 (200).

[20] S. Foner. Versatile and sensitive vibrating-sample magnetometer. *Rev. Sci. Instrum*. **30**, 548–557 (1959).

[21] N. Nagaosa, J. Sinova, J. Onoda, A.H. MacDonald, and N. P. Ong. Anomalous Hall effect. *Rev. Mod. Phys.* **82**, 1539-1592 (2010).

[22] T. L. Gilbert. A Lagrangian formulation of the gyromagnetic equation of the magnetic field. *Phy. Rev.* **100**, 1243 (1955).

[23] R. F. L. Evans, W. J. Fan, P. Chureemart, T. A. Ostler, M. O. A. Ellis, and R. W. Chantrell. Atomistic spin model simulations of magnetic nanomaterials.*J. Phys: Condens. Matter.* **26** 103202 (2014).

[24] W.F. Brown, Jr., Micromagnetics, Wiley Interscience, New York, 1963.

[25] M. J. Donahue and D.G. Porter, Exchange energy formulations for 3d micromagnetics. *Physica B* **343**, 177–183 (2004).

[26] T. Fischbacher, M. Franchin ; G. Bordignon, and H. Fangohr. A Systematic Approach to Multiphysics Extensions of Finite-Element-Based Micromagnetic Simulations: Nmag. *IEEE Trans. Magn.* **43**, 2896-2898 (2007).

[27] OOMMF User's Guide, Version 1.0. M.J. Donahue and D.G. Porter Interagency Report NISTIR 6376,National Institute of Standards and Technology, Gaithersburg, MD (Sept 1999).

[28] M. Mansuripur. Magnetization reversal dynamics in the media of magneto-optical recording. *J. Appl. Phys*. **63**, 5809 (1988).

[29] M. Mansuripur, R. Giles, and G, Patterso. Coercivity of domain-wall motion in thin films of amorphous rare-earth–transition-metal alloys. *J. Appl. Phys*. **69**, 4844 (1991).

[30] C. T. Ma, X. Li, and S. J. Poon. Micromagnetic simulation of ferrimagnetic TbFeCo films with exchange coupled nanophases. *J. Magn. Mater.* **417**, 197-202 (2016).

[31] V. Skumryev, S. Stoyanov, Y. Zhang, G. Hadjipanayis, D. Givord, and J. Nogués. Beating the superparamagnetic limit with exchange bias. *Nature* **423,** 850–853 (2003).

[32] E. Lage, C. Kirchhof, V. Hrkac, L. Kienle, R. Jahns,, R. Knöchel, E. Quandt, and D. Meyners. Exchange biasing of magnetoelectric composites. *Nat. Mater.* **11,** 523–529 (2012).

[33] J. C. S. Kools. Exchange-biased spin-valves for magnetic storage. *IEEE Trans. Magn.* **32,** 3165–3184 (1996).

[34] A. P. Malozemoff. Random-field model of exchange anisotropy at rough ferromagnetic- antiferromagnetic interfaces. *Phys. Rev. B* **35,** 3679–3682 (1987).

[35] W. Kuch, L. I. Chelaru, F. Offi, J. Wang, M. Kotsugi, and J. Kirschner. Tuning the magnetic coupling across ultrathin antiferromagnetic films by controlling atomic-scale roughness. *Nat. Mater.* **5,** 128–133 (2006).

[36] M. Ali, C. H. Marrows, M. Al-Jawad, B. J. Hickey, A. Misra, U. Nowak, and K. D. Usadel. Antiferromagnetic layer thickness dependence of the IrMn/Co exchange-bias system. *Phys. Rev. B* **68,** 214420 (2003).

[37] N. Teichert, A. Boehnke, A. Behler, B. Weise, A. Waske, and A. Hütten. Exchange bias effect in martensitic epitaxial Ni-Mn-Sn thin films applied to pin CoFeB/MgO/CoFeB magnetic tunnel junctions. *Appl. Phys. Lett.* **106,** 192401 (2015).

[38] M. Estrader, A. López-Ortega, S. Estradé, I. V. Golosovsky, G. Salazar-Alvarez, M. Vasilakaki, K. N. Trohidou, M. Varela, D. C. Stanley, M. Sinko, M. J. Pechan, D. J. Keavney, F. Peiró, S. Suriñach, M. D. Baró, and J. Nogués. Robust antiferromagnetic coupling in hard-soft bi-magnetic core/shell nanoparticles. *Nat. Commun.* **4,** 2960 (2013).

[39] D. J. Webb, A. F. Marshall, A. M. Toxen, T. H. Geballe, and R. M. White. Observation of giant exchange anisotropy. *IEEE Trans. Magn.* **24,** 2013–2015 (1988).

[40] S. Romer, M. A. Marioni, K. Thorwarth, N. R. Joshi, C. E. Corticelli, H. J. Hug, S. Oezer, M. Parlinska-Wojtan, and H. Rohrmann. Temperature dependence of large exchange-bias in TbFe-Co/Pt. *Appl. Phys. Lett.* **101,** 222404 (2012).

[41] S. Y. Dong, J. Y. Chen, Z. D. Han, Y. Fang, L. Zhang, C. L. Zhang, B. Qian, and X. F. Jiang. Intermartensitic Transformation and Enhanced Exchange Bias in Pd (Pt) -doped Ni-Mn-Sn alloys. *Sci. Rep.* **6**, 25911 (2016).

[42] A. K. Nayak, M. Nicklas, S. Chadov, P. Khuntia, C. Shekhar, A. Kalache, M. Baenitz, Y. Skourski, V. K. Guduru, A. Puri, U. Zeitler, J. M. D. Coey, and C. Felser. Design of compensated ferrimagnetic Heusler alloys for giant tunable exchange bias. *Nat. Mater.* **14**, 679-684 (2015).

[43] M. Vasilakaki, and K. N. Trohidou. Numerical study of the exchange-bias effect in nanoparticles with ferromagnetic core/ferrimagnetic disordered shell morphology *Phys. Rev. B* **79**, 144402 (2009).

[44] H. Oezelt, A. Kovacs, F. Reichel, J. Fischbacher, S. Bance, M. Gusenbauer, C. Schubert, M. Albrecht, and T. Schrefla. Micromagnetic simulation of exchange coupled ferri-/ferromagnetic heterostructures. *J Magn. Magn. Mater.* **381** 28-33 (2015).

[45] H. Oezelt, A. Kovacs, F. Reichel, P. Wohlhüter, E. Kirk, D. Nissen, P. Matthes, L. J. Heyderman, M. Albrecht, and T. Schrefla, Micromagnetic simulation of

exchange coupled ferri-/ferromagnetic composite in bit patterned media. *J. Appl. Phys*. **117**, 17E501 (2015).

[46] M. Ziese, R. Höhne, A. Bollero, H.-C. Semmelhack, P. Esquinazi, and K. Zimmer, Size and shape dependence of the exchange-bias field in exchange-coupled ferrimagnetic bilayers, Eur. Phys. J. B **45**, 223-230 (2005).

[47] J. P. Zimmermann, G. Bordignon, R. P. Boardman, T. Fischbacher, H. Fangohr, K. N. Martin, G. J. Bowden, A. A. Zhukov, and P. A. J. de Groot. Micromagnetic simulation of the magnetic exchange spring system in $DyFe_2/YFe_2$. *J. Appl. Phys*. **99**, 08B904 (2006).

[48] J. P. Zimmermann, K. Martin, G. Bordignon, M. Franchin, R. C.C. Ward, G. J. Bowden, P. A.J. de Groot, and H. Fangohra, Magnetic switching modes for exchange spring systems $ErFe_2/YFe_2/DyFe_2/YFe_2$ with competing anisotropies. *J. Magn. Magn. Mater*. **321** 2499-2507 (2009).

[49] X. Liu, T. Kanazawa, S. Li, and A. Morisako, Negative coercivity and spin configuration in Ni/TbFeCo/Ni trilayers. *IEEE Trans. Magn*. **45**, 4100 (2009).

[50] X. Li, C. T. Ma, J. Lu, A. Devaraj, S. R. Spurgeon, R. B. Comes, and S. J. Poon. Exchange bias and bistable magneto-resistance states in amorphous TbFeCo thin films. Appl. Phys. Lett. **108**, 012401 (2016).

[51] N.F. Mott and L. Friedman. Metal-insulator transitions in VO_2, Ti_2O_3 and $Ti_{2-x}V_xO_3$. *Phil. Mag*. **30**, 389-402 (1974).

[52] A. Zylbersztejn and N. F. Mott. Metal-insulator transition in vanadium dioxide. *Phys. Rev. B* **11** ¸4383 (1975).

[53] M. Rini, A. Cavalleri, R. W. Schoenlein, R. Lopez, L. C. Feldman, R. F. Haglund, L. A. Boatner, and T. E. Haynes. Photoinduced phase transition in VO_2 nanocrystals: ultrafast control of surface-plasmon resonance. *Opt. Lett*. **30**, 558 (2005).

[54] M. Dragonman, A. Cismaru, H. Hartnagel, and R. plana. Reversible metal-semiconductor transitions for microwave switching applications. *Appl. Phys. Lett*. **88**, 073503 (2006).

[55] H.-T. Kim, B.-G. Chae, D.-H. Youn, S.-L. Maeng, G. Kim, K.-Y. Kang, and Y.-S. Lim. Mechanism and observation of Mott transition in VO2-based two- and three-terminal devices. *New. J. Phys*. **6,** 52 (2004).

[56] H.-T. Kim, B.-G. Chae, D.-H. Youn, G. Kim, K.-Y. Kang, S.-J. Lee, K. Kim, and Y.-S. Lim. Raman study of electric-field-induced first-order metal-insulator transition in VO_2-based devices. *Appl. Phys. Lett*. **86,** 242101 (2005).

[57] E. Strelcov, Y. Lilach, and A. Kolmakov. Gas Sensor Based on Metal−Insulator Transition in VO_2 Nanowire Thermistor. *Nano Lett* **9**, 2322 (2009).

[58] F. J. Morin. Oxides Which Show a Metal-to-Insulator Transition at the Neel Temperature. *Phys. Rev. Lett.* **3,** 34 (1959).

[59] J. M. Atkin, S. Berweger. E. K. Chavez, M. B. Raschke, J. Cao, W. Fan, and J. Wu. Strain and temperature dependence of the insulating phases of VO_2 near the metal-insulator transition. *Phys. Rev. B.* **85**, 020101(R) (2012).

[60] J. H. Park, J. M. Coy, T. S. Kasirga, C. Huang, Z. Fei, S. Hunter, and D. H. Cobden. Measurement of a solid-state triple point at the metal–insulator transition in VO_2. *Nature* **500**, 431-434 (2013).

[61] E. Abreu, M. Liu, J. Lu, K. G. West, S. Kittiwatanakul, W. Yin, S. A. Wolf, and R. D. Averitt. THz spectroscopy of VO_2 epitaxial films: controlling the anisotropic properties through strain engineering. *New. J. Phys.* **14,** 083026 (2012).

[62] M. Liu, H.Y. Hwang, H. Tao, A. C. Strikwerda, K. Fan, G. R. Keiser, A. J. Sternbach, K. G. West, S. Kittiwatanakul, J. Lu, S. A. Wolf, F. G. Omenetto, X. Zhang, K. A. Nelson, and R. D. Averitt. Terahertz-field-induced insulator-to-metal transition in vanadium dioxide metamaterial. *Nature* **487,** 345 (2012).

[63] S. Kittiwatanakul, S. A. Wolf, and J. Lu. Large epitaxial bi-axial strain induces a Mott-like phase transition in VO_2. *J. Appl. Phys*. **105**, 073112 (2014).

[64] J. de la Venta, S. Wang, J. G. Ramirez, and I. K. Schuller. Control of magnetism across metal to insulator transitions. *Appl. Phys. Lett.* **102**, 122404 (2013).

[65] J. de la Venta, S. Wang, T. Saerbeck, J. G. Ramirez, and I. Valmianski. Coercivity enhancement in V_2O_3/Ni bilayers driven by nanoscale phase coexistence. *Appl. Phys. Lett.* **104**, 062410 (2014).

[66] S. S. Nkosi, S. Lafane, B. N. Masina and O. M. Ndwandwe. The control of magnetism near metal-to-insulator transitions of VO2 nanobelts. *J. Alloys Compd.* **689**, 313 (2016).

[67] V. G. Harris, K. D. Aylesworth, B. N. Das, W. T. Elam, and N. C. Koon. Structural origins of magnetic anisotropy in sputtered amorphous Tb-Fe films. *Phys, Rev. Lett*. **69,** 1939 (1992).

[68] X. Yan, M. Hirscher, T. Egami, and E. E. Marinero. Direct observation of anelastic bond-orientational anisotropy in amorphous $Tb_{26}Fe_{62}Co_{12}$ thin films by x-ray diffraction. *Phys. Rev. B* **43,** 9300 (1991).

[69] N. Anuniwat, M. Ding, S. J. Poon, S. A. Wolf, and J. Lu. Strain-induced enhancement of coercivity in amorphous TbFeCo films *J. Appl. Phys.* **113**, 043905 (2013).

[70] M. Ali, R. Watts. Measurement of saturation magnetostriction using novel strained substrate techniques and the control of the magnetic anisotropy. *J. Magn. Magn. Meter.* **202**, 85 (1999).

[71] B.D. Cullity, *Introduction to Magnetic Materials*, Addison-Wesley, Reading, MA, p. 274 (1972).

[72] U. K. Rößler, A. N. Bogdanov, and C. Pfleiderer. Spontaneous skyrmion ground states in magnetic metals. *Nature* **442**, 797–801 (2006).

[73] J. Sampaio, V. Cros, S. Rohart, A. Thiaville, and A. Fert. Nucleation, stability and current-induced motion of isolated magnetic skyrmions in nanostructures. *Nat. Nanotechnol.* **8**, 839-844 (2013).

[74] W. Jiang, P. Upadhyaya, W. Zhang, G. Yu, M. B. Jungfleisch, F. Y. Fradin, J. E. Pearson, Y. Tserkovnyak, K. L. Wang, O. Heinonen, S. G. E. te Velthuis, and A. Hoffmann. Blowing magnetic skyrmion bubbles. *Science* **349**, 283–286 (2015).

[75] N. Romming, C. Hanneken, M. Menzel, J. E. Bickel, B. Wolter, K. von Bergmann, A. Kubetzka, and R. Wiesendanger. Writing and deleting single magnetic skyrmions. *Science* **341**, 636–639 (2013).

[76] N. Romming, A. Kubetzka, C. Hanneken, K. von Bergmann, and R. Wiesendanger. Field-dependent size and shape of single magnetic skyrmions. *Phys. Rev. Lett.* **114**, 177203 (2015).

[77] O. Boulle, J. Vogel, H. Yang, S. Pizzini, D. de Souza Chaves, A. Locatelli, T. O. Menteş, A. Sala, L. D. Buda-Prejbeanu, O. Klein, M. Belmeguenai, Y. Roussigné, A. Stashkevich, S. M. Chérif, L. Aballe, M. Foerster, M. Chshiev, S. Auffret, I. M. Miron, and G. Gaudin. Room-temperature chiral magnetic skyrmions in ultrathin magnetic nanostructures. *Nat. Nanotechnol.* **11**, 449-454 (2016).

[78] I. Dzyaloshinsky. A thermodynamic theory of weak ferromagnetism of antiferromagnetics. *J. Phys. Chem. Solids* **4**, 241–255 (1958).

[79] T. Moriya. Anisotropic superexchange interaction and weak ferromagnetism. *Phys. Rev.* **120**, 91–98 (1960).

[80] S. Mühlbauer, B. Binz, F. Jonietz, C. Pfleiderer, A. Rosch, A. Neubauer, R. Georgii, and P. Böni. Skyrmion Lattice in a Chiral Magnet. *Science* **323**, 915-919 (2009).

[81] X. Z. Yu, N. Kanazawa, Y. Onose, K. Kimoto, W. Z. Zhang, S. Ishiwata, Y. Matsui, and Y. Tokura. Near room-temperature formation of a skyrmion crystal in thin-films of the helimagnet FeGe. *Nat. Mater.* **10**, 106–109 (2011).

[82] R. Tolley, S. A. Montoya, and E. E. Fullerton. Room-temperature observation and current control of skyrmions in Pt/Co/Os/Pt thin films. *Phys. Rev. Mater.* **2**, 044404 (2018).

[83] S. Woo, K. Litzius, B. Krüger, M.-Y. Im, L. Caretta, K. Richter, M. Mann, A. Krone, R. M. Reeve, M. Weigand, P. Agrawal, I. Lemesh, M.-A. Mawass, P. Fischer, M. Kläui, and G. S. D. Beach. Observation of room-temperature magnetic skyrmions and their current-driven dynamics in ultrathin metallic ferromagnets. *Nat. Mater.* **15**, 501–506 (2016).

[84] S. Woo, K. M. Song, X. Zhang, Y. Zhou, M. Ezawa, X. Liu, S. Finizio, J. Raabe, N. J. Lee, S.-I. Kim, S.-Y. Park, Y. Kim, J.-Y. Kim, D. Lee, O. Lee, J. W. Choi, B.-C. Min, H. C.l Koo, and J. Chang. Current-driven dynamics and inhibition of the skyrmion Hall effect of ferrimagnetic skyrmions in GdFeCo films. *Nat. Commun.* **9**, 959 (2018).

[85] M. O. A. Ellis, T. A. Ostler, and R. W. Chantrell. Classical spin model of the relaxation dynamics of rare-earth doped permalloy. *Phys. Rev. B* **86**, 174418 (2012).

[86] C. T. Ma, Y. Xie, H. Sheng, A. W. Ghosh, and S. J. Poon. Robust formation of ultrasmall room-temperature Néel skyrmions in amorphous ferrimagnets from atomistic simulations. *Sci. Rep.* **9**, 9964 (2019).

[87] T. A. Ostler, R. F. L. Evans, R. W. Chantrell, U. Atxitia, O. Chubykalo-Fesenko, I. Radu, R. Abrudan, F. Radu, A. Tsukamoto, A. Itoh, A. Kirilyuk, T. Rasing, and Al. Kimel. Crystallographically amorphous ferrimagnetic alloys: Comparing a localized atomistic spin model with experiments. *Phys. Rev. B* **84,** 24407 (2011).

[88] H. W. Sheng, W. K. Luo, F. M .Alamgir, J. M. Bai, and E. Ma. Atomic packing and short-to-medium-range order in metallic glasses. *Nature* **439**, 419-425 (2006).

[89] N.-H. Kim, D.-S. Han, J. Jung, J. Cho, J.-S. Kim, H. J. M. Swagten, and C.-Y. You. Improvement of the interfacial Dzyaloshinskii-Moriya interaction by introducing a Ta buffer layer *Appl. Phys. Lett*. **107**, 142408 (2015).

[90] J. Cho, N,-H. Kim, S. Lee, J.-S. Kim, R. Lavrijsen, A. Solignac, Y. Yin, D.-S. Han, N. J. J. van Hoof, H. J. M. Swagten, B. Koopmans, and C.-Y. You.Thickness dependence of the interfacial Dzyaloshinskii–Moriya interaction in inversion symmetry broken systems. *Nat. Commun*. **6**, 7635 (2015)

[91] N. H. Kim, J. Jung, J. Cho, D. Han, Y. Yin, J. S.. Kim, H. J. M. Swagten, and C. Y. You. Interfacial Dzyaloshinskii-Moriya interaction, surface anisotropy energy, and spin pumping at spin orbit coupled Ir/Co interface *Appl. Phys. Lett*. **108**, 142406 (2016).

[92] M. Belmeguenai, M. S. Gabor, Y. Roussigné, A. Stashkevich, S. M. Chérif, F. Zighem, and C. Tiusan. Brillouin light scattering investigation of the thickness dependence of Dzyaloshinskii-Moriya interaction in $Co_{0.5}Fe_{0.5}$ ultrathin films *Phys. Rev. B* **93**, 174407 (2016).

[93] M. Belmeguenai, M. S. Gabor, Y. Roussigné, T. Petrisor, Jr., R. B. Mos, A. Stashkevich, S. M. Chérif, and C. Tiusan. Interfacial Dzyaloshinskii-Moriya interaction sign in Ir/Co_2FeAl systems investigated by Brillouin light scattering *Phys. Rev. B* **97**, 054425 (2018).

[94] X. Zhang, Y. Zhou, and M. Ezawa. Antiferromagnetic Skyrmion: Stability, Creation and Manipulation. *Sci. Rep.* **6**, 24795 (2016).

[95] J. Baker and O. A. Tretiakov. Static and Dynamical Properties of Antiferromagnetic Skyrmions in the Presence of Applied Current and Temperature. *Phys. Rev. Lett.* **116**, 147203 (2016).

[96] A. Fert, V. Cros, and J. Sampaio. Skyrmions on the track. *Nat. Nanotechnol.* **8**, 152-156 (2013).

[97] F. Büttner, I. Lemesh,, and G. S. D. Beach. Theory of isolated magnetic skyrmions: From fundamentals to room temperature applications. *Sci. Rep.* **8**, 4464 (2018).

[98] A. Siemens, Y. Zhang, J. Hagemeister, E. Y. Vedmedenko, and R. Wiesendanger. Minimal radius of magnetic skyrmions: statics and dynamics. *New. J. Phys.* **18**, 045021 (2016).

[99] H. Yang, A. Thiaville, S. Rohart, A. Fert, and M. Chshiev. Anatomy of Dzyaloshinskii-Moriya Interaction at Co/Pt Interfaces. *Phys. Rev. Lett.* **118**, 219901 (2017)

[100] C. F. Majkrzak, *et al.*, in *Neutron Scattering from Magnetic Materials* (2005).

[101] B. Maranville, W. Ratcliff II, and P. Kienzle. reductus: a stateless Python data reduction service with a browser front end. *J. Appl. Cryst.* **51**, 1500 (2018).